

# Milky Way Kinematics: Measurements at the Subcentral Point of the Fourth Quadrant

N. M. McClure-Griffiths<sup>1</sup> and John M. Dickey<sup>2</sup>

## ABSTRACT

We use atomic hydrogen (H I) data from the Southern Galactic Plane Survey to study the kinematics of the fourth quadrant of the Milky Way. By measuring the terminal velocity as a function of longitude throughout the fourth Galactic quadrant we have derived the most densely sampled rotation curve available for the Milky Way between  $3 \leq R \leq 8$  kpc. We determine a new joint rotation curve fit for the first and fourth quadrants, which can be used for kinematic distances interior to the Solar circle. From our data we place new limits on the peak to peak variation of streaming motions in the fourth quadrant to be  $\sim 10$  km s<sup>-1</sup>. We show that the shape of the average H I profile beyond the terminal velocity is consistent with gas of three velocity dispersions, a cold component with  $\Delta v = 6.3$  km s<sup>-1</sup>, a warmer component with  $\Delta v = 12.3$  km s<sup>-1</sup> and a fast component with  $\Delta v = 25.9$  km s<sup>-1</sup>. Examining the widths with Galactic radius we find that the narrowest two components show little variation with radius and their small scale fluctuations track each other very well, suggesting that they share the same cloud-to-cloud motions. The width of the widest component is constant until  $R < 4$  kpc, where it increases sharply.

*Subject headings:* ISM: kinematics and dynamics — Galaxy: kinematics and dynamics — radio lines: ISM

---

<sup>1</sup>Australia Telescope National Facility, CSIRO, PO Box 76, Epping NSW 1710, Australia; naomi.mcclure-griffiths@csiro.au

<sup>2</sup>School of Mathematics and Physics, University of Tasmania, Private Bag 21, Hobart TAS 7001, Australia; john.dickey@utas.edu.au

## 1. Introduction

From the first detection of the atomic hydrogen (H I) spectral line in 1951, the  $\lambda 21$ -cm line has been used as a probe of the kinematics of the interstellar medium (ISM) in the Milky Way and the rotation of the Galaxy. The rotation curve of the Milky Way has been a long-standing topic of study with important implications for models of the structure, mass distribution and dynamics of the Galaxy. In one of the earliest studies of the rotation curve, Kwee, Muller, & Westerhout (1954) noticed irregular depressions in the rotation curve of the first Galactic quadrant, which they attributed to a lack of H I between spiral arms. We now understand that H I emission does not give a good indication of gas density and therefore the dips do not reflect density effects, but instead the kinematics of the H I line provide a direct probe of the dynamical effects of spiral structure. In particular, the spiral arms produce deviations, both positive and negative, away from circular rotation that are responsible for the irregularities observed in the rotation curves of the inner Galaxy (Kerr 1962; Shane & Bieger-Smith 1966). These departures from circular rotation have been reasonably well explained by both linear and non-linear spiral density wave theories (Lin et al. 1969; Roberts 1969).

Interior to the Solar circle, every line of sight passes a single subcentral point where it is closest to the Galactic Center and where its projection on the Galactic plane is tangent to a circular orbit around the Galactic Center. At the subcentral point the measured radial velocity of the H I line reaches its most extreme value, called the terminal velocity. In the first Galactic quadrant the terminal velocity is the most positive velocity in H I spectra, whereas in the fourth Galactic quadrant it is the most negative velocity. By measuring the terminal velocity along all lines of sight between Galactic longitudes  $-90^\circ$  and  $+90^\circ$  it is possible to derive a measurement of the rotation curve of the inner Galaxy along the “locus of subcentral points”.

The shape of the H I velocity profile beyond the terminal velocity can tell us about the random motions of H I in the Galaxy. Gas at these velocities is forbidden by Galactic rotation and therefore gives us information about the distribution of H I cloud velocities at the subcentral point. Kulkarni & Fich (1985) employed this technique in an analysis to confirm the existence of two populations of H I clouds, those with a velocity dispersion on the order of  $7\text{--}9 \text{ km s}^{-1}$  as found by Burton (1976) and Liszt (1983) and a second population with a much larger velocity dispersion of  $\sim 35 \text{ km s}^{-1}$ . The Kulkarni & Fich (1985) observations towards  $l = 30^\circ$  of a population of “fast” clouds confirmed earlier work by Radhakrishnan & Srinivasan (1980) and Anantharamaiah et al. (1984) that had originally identified this population of intermediate velocity H I clouds towards the Galactic Center and toward H II regions, respectively.

This is the first paper in a series about the kinematics of the inner Milky Way. In this paper we develop a new technique for measuring the H I terminal velocity. We apply this technique to new, high resolution H I data from the Southern Galactic Plane Survey (SGPS; McClure-Griffiths et al. 2005) to determine the H I terminal velocity along the locus of subcentral points in the fourth quadrant of the Milky Way. The SGPS data have an angular resolution of  $130''$ , which far exceeds the resolution of any previous surveys used to explore H I kinematics at the terminal velocity. From the run of terminal velocities we determine a rotation curve for the inner Galaxy. We also use these data to explore the kinematics of the neutral hydrogen near the subcentral point. The organization of this paper is as follows: in §3 we describe the technique we have used with the SGPS to determine the terminal velocity curve and discuss the advantages of using a high resolution survey for terminal velocity analysis. In §4.3 we use the SGPS terminal velocity curve to derive the rotation curve for the fourth quadrant and we compare these data with a published rotation curve of the first quadrant. In §4.3.1 we derive a new fit to the rotation curve of the inner Galaxy incorporating data from both the first and fourth Galactic quadrants and in §4.3.2 we discuss the magnitude of the velocity residuals and their relationship to spiral structure. Finally, in §5 we discuss the shape of the H I velocity profile beyond the terminal velocity and touch on its implications for the kinematics of diffuse H I.

## 2. Data

The H I data discussed here were obtained as part of the Southern Galactic Plane Survey (SGPS; McClure-Griffiths et al. 2005). The SGPS is an H I spectral line and 21-cm continuum survey of the Galactic plane between longitudes  $253^\circ \leq l \leq 358^\circ$  (SGPS I) and  $5^\circ \leq l \leq 20^\circ$  (SGPS II) and with latitude coverage of  $|b| \leq 1.4$ . The observations and analysis of these data are described in full detail in McClure-Griffiths et al. (2005). The SGPS data were obtained with the Australia Telescope Compact Array (ATCA) and the Parkes radio telescope and were combined to provide images with sensitivity to all angular scales from  $130''$  to several degrees. The SGPS I H I data have been released as a series of overlapping sub-cubes, each covering  $11^\circ$  of longitude and  $2.89$  of latitude with an angular resolution of  $130''$  and a spectral resolution of  $0.82 \text{ km s}^{-1}$ . The noise in the line free channels of the H I cubes is  $1.6 \text{ K}$ .

### 3. Measuring the Terminal Velocity

On each line of sight near the Galactic plane circular rotation gives a velocity relative to the Local Standard of Rest (LSR) that projects on the line of sight as

$$v_{LSR} = R_0 \sin l (\omega - \omega_0) \cos b, \quad (1)$$

where  $\omega$  is the angular velocity of Galactic rotation at the point of interest, and  $\omega_0$  is the corresponding Galactic rotation of the solar circle ( $R = R_0$ ). Throughout this paper we adopt the IAU standard values for the distance to the Galactic Center,  $R_0 = 8.5$  kpc, and  $\omega_0 = \Theta_0/R_0 = 220 \text{ km s}^{-1}/8.5 \text{ kpc}$ . The terminal velocity is defined as the extreme velocity on any line of sight at  $b \approx 0^\circ$ , which occurs at the subcentral or tangent point where the galactocentric radius is  $R = R_0 \sin l$  for any realistic rotation curve. The projected radial component of this maximum allowed circular rotation velocity gives the rotation curve of the Galaxy,  $\omega(R)$ , or alternatively  $\Theta(R)$ . At this position the helio-centric distance,  $r$ , is determined from geometry simply as  $r = R_0 \cos l$ .

For cold gas in a perfectly circular orbit, and in the absence of turbulent motions, the H I spectrum would drop to zero at velocities beyond the terminal velocity (in the fourth Galactic quadrant: at more negative velocities). However, H I and other real spectral line tracers do not drop discontinuously to zero for velocities beyond the terminal velocity because the gas has a measurable thermal velocity width as well as bulk random motions. For most of the gas in the Milky Way these random motions are roughly 5% or less of the circular velocity (Burton 1976), so line profiles near latitude zero drop quite sharply near the terminal velocity. Analysis of the shape of the H I velocity profile beyond the terminal velocity can give us information about the random motions of the gas in the region near the subcentral point. Similarly, understanding the distribution of random velocities helps refine the method of estimating the extreme allowed circular rotation velocity from the line profiles. Here we carefully fit the terminal velocity profile to reveal both.

A variety of methods have been employed to define a point along the velocity profile as the terminal velocity. For example, Kerr (1962) defined the terminal velocity,  $V_{LSR}$ , as the last peak of the profile, whereas Sinha (1978) used a relative definition in which the terminal velocity is where the line profile crosses a threshold set at half the value of the most extreme allowed velocity emission peak. Shane & Bieger-Smith (1966) and Celnik, Rohlfs, & Braunsfurth (1979) derived functional forms for the shape of the H I profile and the terminal velocity and fit their model profiles with a defined terminal velocity to the observed profiles to define the exact drop off. More recently, Malhotra (1995) used an absolute brightness temperature threshold to define the terminal velocity. We have employed a compromise technique, which starts with an absolute brightness temperature threshold to

adjust the velocity profile followed with function fitting to define the exact velocity of the underlying discontinuity, independent of threshold choice. We made two passes through the data in an effort to avoid the effects of an arbitrary choice of measurement parameters.

### 3.1. Continuum Blanking

An important advantage of a high angular resolution survey like the SGPS is that the effects of absorption of continuum emission from beyond the subcentral point can be removed from the data. When observed toward a bright continuum source, the H I spectrum shows a mixture of emission and absorption at all velocities. The absorption can overwhelm the emission, particularly near the subcentral point where velocity crowding causes a long segment of the line of sight to pile up in the spectrum near the terminal velocity. For a low resolution survey, such as one observed with a single dish telescope, absorbed and non-absorbed pixels are averaged with a weighting given by the beam shape.

The blended emission and absorption in a low resolution survey leads to an underestimate of the maximum velocity, as absorption towards continuum sources in the beam will tend to flatten the steep “cliff edge” of the emission profile near the terminal velocity. A clear example of this effect is shown in Figure 1, which shows two spectra at the same longitude at two different latitudes ( $b=\pm 0^{\circ}2, l = 305^{\circ}25$ ) where the first has bright continuum in the background and the second does not. The effect of the absorption is to reduce the height of the emission, in extreme cases the brightness temperature can even go negative because the continuum has been subtracted from the SGPS data. This causes the apparent rotation velocity, whether defined by a threshold or by profile fitting, to be biased to unrealistically low values wherever there is bright background continuum emission. To avoid this bias in our analysis we have used the SGPS continuum images (Haverkorn et al. 2006) to blank all pixels with  $T_{cont} > 0.5$  K. Overall we blank about 10% of the survey area. Without blanking we find that the measured terminal velocities show more scatter from one longitude to the next. Single dish surveys are not able to do this because their much larger beam size irrevocably blends the spectra toward continuum sources with the surrounding emission spectra, reducing the measured terminal velocity.

### 3.2. Thresholding on Latitude Averages

After continuum blanking our first step is to chose a brightness temperature threshold that selects a velocity that is part way down the steepest slope in the emission profile, the

“cliff” just past the subcentral point velocity. An individual spectrum is rather noisy ( $\sigma_T = 1.6$  K) so it is necessary to perform some kind of latitude average before thresholding. A simple average over latitude would return the mean of this distribution. Alternatively we could work with the median, i.e. the 50th percentile  $T_b$ , or some other value of  $T_b$  defined from this distribution such as the 25th or 75th percentile. Because all latitudes are included in constructing the spectrum any of these statistics could be used on the distribution of  $T_b$  at each velocity to construct a spectrum that has relatively low noise.

The SGPS interferometer data latitude coverage of  $\pm 1^\circ$  corresponds to 55 times the beam width, or about 70 independent points for each beam width in longitude. The scale height,  $h$ , of the H I gas in the inner Galaxy is about  $\pm 150$  pc in  $z$  (Dickey & Lockman 1990), which gives  $\pm 1^\circ$  angular width at the nominal galactocentric distance  $R_0 = 8.5$  kpc. Thus all lines of sight with  $|b| < 0.5^\circ$  pass the subcentral point when they are still well inside the H I layer ( $|z| \ll h$ ), so all spectra at the same longitude show roughly the same sharp drop beyond the subcentral point velocity. Corrections to the projected rotation velocity to account for the non-zero latitude, both due to the reduced projection of the circular rotation velocity vector along the line of sight and due to departures from cylindrical rotation of the gas above or below the mid-plane at the subcentral point, are insignificant ( $\sim 10^{-3}$ ) for latitudes  $|b| < 1^\circ$ . For the terminal velocity analysis described here we have used only spectra within  $|b| < 0.5^\circ$ , so the effect of the finite scale height is very slight. We can therefore consider any set of spectra at the same longitude as realizations from the same statistical ensemble, differing in their profile shapes due to small scale random motions near the subcentral point, but all having the same underlying rotation velocity.

For each longitude we have used the many independent spectra at different latitudes to study the distribution function of H I emission brightness temperature,  $T_b$ , at each velocity. An example of one such distribution function of  $T_b$  at  $-0.5^\circ < b < +0.5^\circ$ ,  $l = 305.25$  and  $v = -61.83$  km s $^{-1}$  is shown in Figure 2. This is the velocity where the mean of the distribution crosses the 10 K threshold, i.e. the most negative velocity with mean  $T_b(v) > 10$  K. The positions of all four statistics, mean, median, 25th and 75th percentile are marked on Figure 2. We have used all four statistics to determine the velocity of threshold crossing. We have carried the velocities found with each statistic through the second part of the analysis, as discussed in §3.3, to establish which statistic is most robust.

Whatever the choice of threshold in  $T_b$  and the statistic chosen to determine the average  $T_b(l, v)$  from  $T_b(l, b, v)$ , after continuum blanking and averaging we have a function  $v_t(l)$ , which is the velocity of threshold crossing. This is not the rotation curve, but it is the first step toward the rotation curve. Using this function, we shifted all spectra in the survey by the velocity corresponding to their longitude,  $v_t(l)$ , and then computed an  $l$ - $v$  diagram

based on the average in latitude. By shifting the spectra in velocity by  $v_t(l)$  we removed the gross effects of Galactic rotation so that we could average spectra in longitude. Figure 3 is a terminal velocity profile averaged over the longitude range  $272^\circ \leq l \leq 340^\circ$ . The velocity scale of Figure 3 reflects the shift so that  $0 \text{ km s}^{-1}$  corresponds to the threshold crossing,  $v_t(l)$ . The subcentral point is at a positive velocity somewhat offset from  $v_t$ . The value of the offset depends on the threshold choice, and the choice of statistic (mean, median, or other percentile) used for the latitude averaging. In the next section we describe how we determine the offset to the subcentral point by fitting complementary error functions,  $\text{erfc}(v)$ , to the terminal velocity profile.

### 3.3. Error Function Fitting of the Terminal Velocity Shape

The second step in determining the terminal velocity was to fit the shifted spectral averages with a functional form to establish a robust velocity for the subcentral point. For cold gas with no velocity dispersion the H I profile would drop sharply at the terminal velocity. However, the H I profile does not show the ideal edge of a Heaviside step function, but is instead smoothed out by the velocity dispersion of the gas. A commonly used technique to find the edge of a step function blended by some natural dispersion is to fit a complementary error function,  $\text{erfc}$ , which returns the position of the edge and as well as the width of the blending process. The relationship between the step function and the error function can be seen clearly if we consider the Heaviside step function as the limit of a complementary error function

$$H_{v_o}(v) = \frac{1}{2} \lim_{\Delta v \rightarrow 0} \text{erfc}((v_o - v)/\Delta v), \quad (2)$$

where  $v_o$  is the velocity offset of the edge and  $\Delta v$  characterizes the deviation from an ideal edge. The use of an error function to fit the H I profile beyond the terminal velocity is not without precedent, Kulkarni & Fich (1985) used this form in their exploration of the velocity dispersion of H I. In this application, the width  $\Delta v$ , relates to the Gaussian dispersion as  $\Delta v = \sqrt{2}\sigma_v$ .

There is also some physical justification for using an error function to fit the H I line profile. Beyond the terminal velocity,  $v_{LSR}$ , we expect that the gas must become optically thin, meaning that the brightness temperature becomes proportional to the column density of atoms in each velocity interval,  $\delta v$ . If the density of gas at allowed velocities is a constant,  $n_o$ , then the brightness temperature at a velocity beyond the terminal velocity ( $v < v_o$ , where  $v_o < 0$  for the fourth quadrant) for which the gas is optically thin is

$$T_b(v) \delta v = \frac{n_o}{C_o} \int_{-v}^{\infty} \left| \frac{dv'}{dr} \right|^{-1} f(v - v') dv', \quad (3)$$

where the upper limit on the velocity integral is not really infinity, but the range of allowed velocities is so wide on most lines of sight that the upper limit does not matter. The function,  $f(v - v')$ , is the velocity distribution function of H I atoms contributing to the emission, assumed to be a Gaussian. The constant  $C_o$  is the familiar  $1.823 \times 10^{18} \text{ cm}^{-2} (\text{K km s}^{-1})^{-1}$  conversion factor between brightness temperature and column density for the  $\lambda 21\text{-cm}$  line. Finally,  $|dv'/dr|$  is the magnitude of the inverse of the velocity gradient along the line of sight, evaluated at position  $r$  that has radial velocity  $v'$ . As we can see, Equation 3 bears a strong resemblance to the complementary error function but for the  $|dv'/dr|$  term inside the integral. Celnik et al. (1979) showed that for a smooth rotation curve the velocity gradient,  $dv/dr$ , near the terminal velocity gradient is small and directly proportional to distance,  $r$  with a slope given by the local value of Oort's constant over  $R$ . At the subcentral point the velocity gradient crosses zero, such that the absolute value of the velocity gradient has a sharp discontinuity at the subcentral point. For optical depths  $\tau \ll 1$ , this sharp discontinuity should result in a sharp peak in the H I profile at the terminal velocity. In fact, we generally do not observe a sharp peak, but a smoothly rolled off velocity profile, which suggests saturation in the line profile near the subcentral point. The effects of saturation and spatial variations in the density appear to mask any correlation between the magnitude of the velocity gradient and the amplitude of the emission at the terminal velocity, such that the erfc function scales to connect smoothly with  $T_b(v_o)$ , whatever it is. Thus if we make the assumption that for low longitudes the term  $n_o |dv'/dv|^{-1}$  is roughly a constant near the subcentral point then it can be taken out of the integral, leaving the complementary error function for the velocity dependence of the line profile beyond the terminal velocity. Fitting this function reveals both the terminal velocity and the width of the underlying Gaussian distribution of velocities.

As was pointed out by Kulkarni & Fich (1985), a single Gaussian for  $f(v)$  is not a good fit to the data. A single Gaussian is unable to fit the sharp drop plus a long tail of emission beyond the terminal velocity. The next most simple functional description of  $T_b(v)$  is the sum of two or three complementary error functions, corresponding to two or three Gaussians of widths,  $\sigma_v$ :

$$T_b(v) = \sum_{i=1}^3 a_i \text{erfc}(-1 * (v - v_o)/\Delta v_i), \quad (4)$$

where the width of the error functions,  $\Delta v_i$ , is related to the original Gaussian width as  $\Delta v_i = \sqrt{2}\sigma_{v_i}$ . The top and bottom panels of Figure 3 show fits of two and three error functions, respectively, to the longitude average of the shifted  $T_b(v)$ . Clearly the low-level emission tail cannot be well fitted by even the sum of two error functions, instead it is necessary to use a sum of three error functions. We discuss the implications of this for H I kinematics in §5 below.



To determine the true terminal velocity at the subcentral point  $v_{LSR} = v_t + v_o$ , we fit error functions to shifted and longitude averaged  $T_b(v)$  profiles to return values for  $v_o(l)$ . The formal fits were done by minimizing the chi-squared for the fit using Powell’s method of minimization (Press et al. 1992). We found that  $v_o(l)$  determined from fitting a sum of two error functions was identical to within 2% to  $v_o(l)$  determined from fitting a sum of three error functions. Therefore, for speed and robustness against noisy spectra we determined  $v_o(l)$  by fitting the sum of only two error functions.

The fitted values for  $v_o(l)$  depend on the threshold value and the statistic used to average the spectra in latitude, but the true terminal velocity,  $v_{LSR}$ , is largely independent of threshold and statistic. This is illustrated in Figures 4 and 5. Figure 4 shows the threshold crossing velocities,  $v_t$ , before and after correction by  $v_o$  for twenty longitude bins between  $l = 340^\circ$  and  $l = 292^\circ$ . The four crosses in each longitude bin are the values of  $v_t$  obtained from the 10 K threshold crossing for each of these four statistics. In each case the outliers are the 25th and 75th percentiles, whereas the median and mean statistics give similar results. Fitting the velocity offset,  $v_o$ , to the corresponding spectrum averages gives different values that usually make up for the difference in the percentiles, so that the sum,  $v_{LSR} = v_t + v_o$  comes out the same for all four statistics. The dotted curve corresponds to  $v_{LSR}$  for the 75th percentile, the dashed curve for the 25th percentile, and the two solid curves for the mean and median. For longitudes  $l \leq 325^\circ$  the scatter among the four values of  $v_t$  is 1 to 2 km s<sup>-1</sup>, but the scatter among the four values of  $v_{LSR}$  is only 0.26 km s<sup>-1</sup>. In this range, the continuous curves on Figure 4 are indistinguishable. For longitudes  $327.5 \leq l \leq 330^\circ$  the points spread apart, but the values of  $v_{LSR}$  have less scatter than  $v_t$ . At all longitudes the values of  $v_{LSR}$  obtained from the mean and median in latitude agree to better than 0.6 km s<sup>-1</sup>, except at  $l = 328.25$  where their difference is 4.6 km s<sup>-1</sup> and at  $l = 338.25$  where the difference is 1.2 km s<sup>-1</sup>. The striking agreement of the values of  $v_{LSR}$  obtained from the different choices of statistics to define  $v_t$  after correction for the offset velocity,  $v_o$ , demonstrates that the erfc fitting effectively removes any bias introduced by the arbitrary choice of statistic for the latitude averaging.

The velocity offset correction also effectively corrects for any bias introduced by the choice of threshold values. This is shown in Figure 5 where we compare  $v_t$  and  $v_{LSR}$ , both derived using longitude averages but with brightness thresholds of 10 K and 20 K. The 20 K threshold reduces the velocity shifts by 3-5 km s<sup>-1</sup>, but this is made up by smaller offsets between the threshold crossing velocity and the edge of the underlying step in the brightness distribution derived from the error function fitting, so that the discrepancy in  $v_{LSR}$  is much smaller. The difference in  $v_{LSR}$  derived using the two thresholds is less than 1 km s<sup>-1</sup> for longitudes  $l \leq 325^\circ$ , and less than 2.5 km s<sup>-1</sup> for longitudes  $l \geq 332.5$ . Overall the adjustment from the erfc fitting does a good job of correcting for bias due to the arbitrary

choice of threshold. The difference in threshold crossing velocity,  $v_t$ , is typically 5 to 15  $\text{km s}^{-1}$  before applying the shift,  $v_o$ , obtained from the erfc fits.

As seen in Eq. 3 and discussed above, the brightness temperature is related to product of the local H I density,  $n_o$  and the inverse of the velocity gradient,  $|dv/dr|^{-1}$ . Because of this relationship there is a danger with a pure threshold method that a localised change in  $n_o$  or  $dv/dr$  could increase the local brightness temperature and hence alter the measured terminal velocity. The velocity offset correction method that we employ provides some robustness against masking density or velocity gradient changes as terminal velocity changes by compensating for variations in the threshold velocity. Our estimates of the offset velocity made by fitting error functions to the terminal velocity profile are dominated by the velocity, rather than the brightness temperature, of the peak of the error function at  $v \approx v_{LSR}$ . Therefore, the value of the threshold, or even its position along the velocity tail, is largely irrelevant to our determination of  $v_{LSR}$  and we are immune to density and velocity gradient effects on  $T_B$ . It is worth noting however, that the offset fitting method does not provide much protection against very large-scale (factor of  $\sim 2$  or more) variations in  $n_o$  or  $dv/dr$  away from the subcentral point which can effectively shift the velocity of the peak back from the terminal velocity. At present there is no method that can resolve these from true variations in the rotational velocity and it remains a limitation of all Milky Way rotation curves.

Thus the final values of  $v_{LSR}$  should be repeatable and independent of the choice of threshold or statistic to within  $0.5 \text{ km s}^{-1}$  for  $l \leq 325^\circ$ , and within  $3 \text{ km s}^{-1}$  for  $l \geq 332.5$ . In the range  $326.5 \leq l \leq 332.5$  there is a discrepancy in the results from the two thresholds that is as large as  $10 \text{ km s}^{-1}$ . Similarly, the range  $327.5 \leq l \leq 330^\circ$  gives a large variation in threshold crossing velocity using the same threshold but different statistics in latitude (see Figure 4). For example, the mean and median for the 10 K threshold give  $v_t = -143.1 \text{ km s}^{-1}$  and  $v_t = -138.3 \text{ km s}^{-1}$ , respectively. The offsets derived from the error function fitting in that case are  $v_o = 24.5 \text{ km s}^{-1}$  and  $v_o = 23.7 \text{ km s}^{-1}$ , which reduce the discrepancy, but only slightly. This appears to be due to abnormal variation in the slope of the profiles beyond the terminal velocity in this region, making the method of latitude averaging, and the choice of threshold, give different results. This is possibly evidence for heightened rate of stirring up random motions in the medium, due to increased star formation activity in the galactocentric radius range  $3.9 \leq R \leq 4.5 \text{ kpc}$ . As discussed below, this is a region where the rotation velocity increases rapidly with R, which may be due to non-circular motions associated with a spiral arm.

## 4. The Terminal Velocity Curve

Using the threshold method and error function fitting we have determined the terminal velocity,  $v_{LSR}$ , for 1000 longitude bins of width  $3'$  between  $l = 339.5^\circ$  and  $l = 272^\circ$ . We used a threshold value of 10 K to determine  $v_t(l)$  and we fit the sum of two error functions for each longitude bin to determine,  $v_o(l)$ . Table 1 gives the measured terminal velocity,  $v_{LSR}$ , and central longitude,  $l$ , for each longitude bin. The terminal velocity curve, together with the values for  $v_o(l)$ , is shown in Figure 6. For clarity we have not plotted the error bars, which should reflect the estimation of the error from on thresholding and fitting described in §3.3.

The longitude range used for this terminal velocity curve analysis has been chosen to avoid extreme non-circular motions associated with the inner 3 kpc of the Galaxy. In order to translate the measured values of  $v_{LSR}$  to a rotation curve we must assume circular rotation along the locus of subcentral points. We know, however, that circular rotation breaks down in most of the very inner Galaxy. At  $R \lesssim 3$  kpc, gas orbits become elliptical because of the dynamical effects of the three kiloparsec arm and the bar (Burton & Liszt 1993; Ferrière et al. 2007). The dynamics of the H I in the innermost region of the Galaxy will be the subject of a future paper and will not be discussed further here.

Automated function fitting produced spurious fits for  $\sim 2\%$  of the longitude bins. Some of these are visible as cusps in the terminal velocity curve at  $l = 306^\circ$ ,  $l = 312^\circ$  and  $l = 320^\circ$  in Fig. 6. Examining the H I datacubes we found that at these three longitudes there are discrete H I clouds  $10\text{-}20 \text{ km s}^{-1}$  beyond the terminal velocity, which disrupt the fitting. These clouds are spatially only marginally resolved, have low brightness temperature features ( $T_b \sim 10 \text{ K}$ ) and FWHM velocity widths of  $\sim 10 \text{ km s}^{-1}$ . They may be similar to the outlying clouds described by Stil et al. (2006). In the remainder of the SGPS H I profiles used in this analysis the high velocity linewings are smooth and do not show small, discrete components. To remove the velocity spikes at  $l = 306^\circ, 312^\circ$  and  $320^\circ$  from the subsequent analysis we have run a median filter with a width of 9 samples across the  $v_o(l)$  values.

### 4.1. Comparison with CO terminal velocities

H I because of its ubiquity is often hailed as an excellent tracer of the terminal velocity curve. However, its ubiquity together with large ( $\sim 5 - 10 \text{ km s}^{-1}$ ) thermal and turbulent line widths can lead to line blending. Because of these limitations, the terminal velocity curve has often been studied from observations of the  $^{12}\text{CO } J = 1 - 0$  transition. Unlike H I, the thermal linewidth of the  $^{12}\text{CO}$  line is typically very small,  $< 1 \text{ km s}^{-1}$  and even the

turbulent width is typically only  $\sim 2 \text{ km s}^{-1}$  (Burton 1976), which reduces the problems of line blending. Because of this  $^{12}\text{CO}$  determined terminal velocity curves should demonstrate less scatter than their H I counterparts. Comparison of  $^{12}\text{CO}$  and H I terminal velocities can test how free our H I terminal velocities are from systematic effects caused by turbulence and line-blending. In Figure 7 we have overlaid values for the recent  $^{12}\text{CO}$  terminal velocity curve measured by Luna et al. (2006) on our H I terminal velocities as a function of  $\sin l$ . The Luna et al. (2006) values are sampled every  $0^\circ.125$  and were selected as the half-intensity point of the extreme velocity peak.

The agreement between the H I and  $^{12}\text{CO}$  datasets is striking; the two curves traces each other extremely well including many of the dips and wiggles. On average the scatter in the  $^{12}\text{CO}$  data points is about three times that of the H I data points. The larger scatter in the CO data may be partially attributed to the fact that these data are less sensitive than the H I data and also that Luna et al. (2006) used a threshold method for determining the terminal velocity. However, it is likely that physical effects relating to the small volume filling factor of CO contribute significantly to the difference in scatter between H I and CO. The low filling factor of CO means that observations at the subcentral point typically detect a very small number of discrete CO clouds. The CO observations are therefore sensitive to the individual velocity dispersions of the CO clouds, rather than an ensemble average as measured with H I. This can lead to a larger scatter for individual measurements. The comparison of these two curves raises confidence that H I is not overly dominated by blending or turbulence and may in fact indicate that H I is a more robust measure of the terminal velocity.

## 4.2. Determining $AR_0$

Oort’s  $A$  constant is an important quantity for probing differential Galactic rotation in the vicinity of the Sun. Although H I data are not able to determine  $A$  directly, terminal velocities have been used to measure the product  $AR_0$ , where

$$v_{LSR} = -2AR_0(1 - |\sin l|) + v'. \quad (5)$$

measured near to the Sun (e.g Gunn et al. 1979). In principle we could determine  $AR_0$  by simply fitting Equation 5 to the SGPS terminal velocities as a function  $\sin l$  plotted in Figure 7. This is best done near the Sun because  $A$  is a locally determined quantity. However, this is complicated enormously by streaming motions both near the Sun and throughout the inner Galaxy, which lead us to fit over large ranges of  $\sin l$  in order to overcome localized non-circular motions. Lin, Yuan, & Roberts (1978) use nonlinear density wave theory to demonstrate that the value obtained for  $AR_0$  depends strongly on the location where it is

measured. From Figure 7 it is clear that although the general trend for the SGPS terminal velocity is linear, there are significant departures from a linear fit. We found that the values determined for  $AR_0$  depend on the range of longitudes used in the fitting. We immediately eliminated data in the range  $\sin l > 0.95$  because the magnitude of the measured terminal velocities at these longitudes ( $\sim 10 \text{ km s}^{-1}$ ) is comparable to the width of the terminal velocity profile as well as any expected deviations due to streaming motions. In Figure 7 we show two fits to the data over different ranges of  $\sin l$ . We found that fits to  $0.8 \leq \sin l \leq 0.95$  return  $AR_0 = 110 \pm 2 \text{ km s}^{-1}$ , which agrees very well with Gunn et al. (1979) and implies  $A = 13 \text{ km s}^{-1} \text{ kpc}^{-1}$  if  $R_0 = 8.5 \text{ kpc}$ . However, fits over a broader range of  $\sin l$  extending up to  $\sin l = 0.35$  return  $AR_0 = 89 \pm 4 \text{ km s}^{-1}$ , which implies  $A = 10.5 \text{ km s}^{-1} \text{ kpc}^{-1}$  if  $R_0 = 8.5 \text{ kpc}$ . Alvarez, May, & Bronfman (1990) found a similar difference between the slope for fits to data up to  $l = 320^\circ$  and for data up to  $l = 340^\circ$  and attributed the difference to anomalous velocities in Carina, as discussed by Humphreys & Kerr (1974). The large range of  $AR_0$  determined within the same data-set reveals just how sensitive the product of these constants is to the location in which it is measured. As warned by Lin et al. (1978) one should exercise extreme caution when determining  $AR_0$  from H I or CO terminal velocity measurements.

Recognising the intrinsic errors in determining  $AR_0$  it is still interesting to compare the range of  $AR_0$  implied by our data to  $A$  measured from proper motions of stars. Comparing our values of  $AR_0 = 89 - 110 \text{ km s}^{-1}$  with the Hipparchos results for  $A$  (Mignard 2000) shows that for  $R_0 = 8.5$  the lower limit of our range is consistent with the  $A$  values derived for hot stars in the disk (e.g.  $A = 10.9 \pm 0.8 \text{ km s}^{-1} \text{ kpc}^{-1}$  for stars of type A0-A5 with  $|b| < 30^\circ$ ), but even our upper limit is smaller than the Hipparchos result for giant stars at all latitudes, which is  $A \simeq 14.7 \pm 1 \text{ km s}^{-1} \text{ kpc}^{-1}$ . Our upper limit value of  $A$  assuming  $R_0 = 8.5 \text{ kpc}$  is also smaller than the conventionally accepted value of  $A = 14.5 \text{ km s}^{-1} \text{ kpc}^{-1}$  (Binney & Tremaine 1987). This low value of  $A$  derived from the H I terminal velocities compared with the locally measured value based on stellar radial velocities and distances supports the mounting evidence that the Galactic Center distance is smaller than the 8.5 kpc assumed here (Reid 1993; Eisenhauer et al. 2005).

### 4.3. Inner Galaxy Rotation Curve

Using terminal velocities measured from the SGPS data and the circular velocity relation that  $\Theta(R) = |v_{LSR}| + \Theta_0 |\sin l|$  we have calculated the rotation curve for  $3 \leq R \leq 8 \text{ kpc}$ . Figure 8 shows the rotation curve for the fourth Galactic quadrant derived from SGPS terminal velocity measurements. Also plotted on this figure are the rotation curve data

points from the first quadrant published by Fich et al. (1989), which were derived from H I data presented by Burton & Gordon (1978). We include on Figure 8 two commonly used rotation curve fits, the one derived for the outer Galaxy by Brand & Blitz (1993) and the one derived for the first quadrant by Burton & Gordon (1978). Note that the Brand & Blitz (1993) fit is almost identical to the Fich et al. (1989) rotation curve fit, determined for the inner and the outer Galaxy.

The general trend of the SGPS rotation curve over the full range of plotted radii is for increasing rotation velocity with increasing galactocentric radius. In addition, there is clearly a great deal of dynamic structure along the locus of subcentral points. The bump at  $R = 3.4$  kpc is attributed to the well-known three kiloparsec arm (van Woerden et al. 1957). This feature is very well traced by the SGPS terminal velocity data but it is clearly not in circular rotation and should not fit by rotation curve models. Other noticeable peaks and troughs in the rotation curve have long been attributed to streaming motions associated with the spiral arms of the Galaxy (Shane & Bieger-Smith 1966; Yuan 1969; Burton 1971). At these locations the assumption of circular rotation breaks down and the terminal velocity curve traces not the overall rotation of the Galaxy, but the dynamical influence of the spiral arms.

From  $R \approx 3.9$  kpc the rotation curve rises rapidly from  $\Theta = 210$  km s<sup>-1</sup> to 225 km s<sup>-1</sup> at  $R \approx 4.4$  kpc. This rise is mirrored in the first quadrant rotation curve, also shown in Fig. 8, although for the first quadrant curve the rise is shifted to larger radii by approximately 100 pc. At  $R \approx 5.7$  kpc there is a very sharp local minimum of  $\Theta = 211$  km s<sup>-1</sup> followed by a smooth rise towards a maximum of 240 km s<sup>-1</sup> near  $R \approx 6.7$  kpc. There is a clear difference between the first and fourth quadrant rotation curves  $R > 7$  kpc. This difference has been given as evidence of anomalous velocities associated with streaming motion Sagittarius-Carina arm at  $l \sim 295^\circ$  (Henderson et al. 1982; Grabelsky et al. 1987). On the other hand, asymmetries between the first and fourth quadrant curves have also been explained by Kerr (1962) and Blitz & Spergel (1991) as evidence for an outward motion of the Local Standard of Rest orbit. If there is an outward motion of the LSR this would apply an offset to the derived rotation curve of  $-2\Pi_o \cos l$ , where  $\Pi_o$  is the magnitude of the outward velocity, estimated to be 14 km s<sup>-1</sup> by Blitz & Spergel (1991). Our current data, because they are restricted to the fourth quadrant, are not sufficient to resolve whether there is an outward velocity of the LSR so we omit this correction for now.

The SGPS data, because of their high angular resolution, allow us to clearly resolve individual features in the rotation curve. Superposed on the large scale features are a multitude of small features with velocity amplitudes  $\sim 2 - 5$  km s<sup>-1</sup>, over length scales of 100 to 200 pc. One such example lies at  $\sim 8$  kpc and can be attributed to the Carina supershell

(Dawson et al. 2006), which has carved a hole out of the disk and disturbed the kinematics near the terminal velocity. Presumably some of the other small scale features can be attributed to discrete objects, but another fraction must represent the random cloud-to-cloud motions near the subcentral point.

#### 4.3.1. A Fit to the Rotation Curve for $3 \leq R \leq 8$ kpc

As seen in Figure 8, neither of the two commonly used rotation curve formulae are good fits to the data. The Brand & Blitz (1993) rotation curve, which is often used for kinematic distance estimates, is not a particularly good representation of both the first and fourth quadrants. That this curve is a poor fit for the inner Galaxy ( $R < R_0$ ) is not surprising as it was derived to fit the outer Galaxy. When plotted over the inner Galaxy it is clear that the Brand & Blitz (1993) fit is much flatter than the data. Similarly, the Burton & Gordon (1978) fit, although a reasonable fit for the first quadrant, is much too steep for the fourth quadrant data. Other rotation curves have been derived specifically for the inner Galaxy, such as Clemens (1985), but this high order polynomial fit was derived to fit data from the locus of subcentral points in the first quadrant. The curve includes fits to the large scale velocity deviations known to be associated with spiral arms and is therefore of limited applicability to other parts of the inner Galaxy.

Here we use both the first and fourth quadrant data together to derive a new fit to the rotation curve appropriate for  $3 \text{ kpc} < R < 8 \text{ kpc}$  at all longitudes. Following Fich et al. (1989) and Brand & Blitz (1993) we fit the data with a variety of functional forms, including first and second-order polynomials and the power law  $\Theta/\Theta_0 = c_1(R/R_0)^{c_2} + c_3$ , where  $c_1$ ,  $c_2$ , and  $c_3$  are the free parameters to be determined by the fit. The fitting was done using a non-linear least-squares algorithm on the combination of the first quadrant and SGPS data, including the standard deviations of each. The standard deviation for the first quadrant velocities is  $\sigma_v = 4.5 \text{ km s}^{-1}$  (Fich et al. 1989; Burton & Gordon 1978). The SGPS standard deviations were derived from the repeatability of the  $v_{LSR}$  determination as discussed in §3.3. We let  $\sigma_v = 1 \text{ km s}^{-1}$  for  $l < 325^\circ$  and  $\sigma_v = 3 \text{ km s}^{-1}$  for  $l > 332.5$  and  $\sigma_v = 10 \text{ km s}^{-1}$  for  $327.5 \leq l \leq 330^\circ$ . All data were additionally weighted according to  $\sin l$  to compensate for the uneven sampling in this domain. Finally, the first quadrant weights were adjusted by the ratio of the number of points in the first and fourth quadrant datasets to compensate for the fact that the SGPS data are much more densely sampled than the first quadrant data. We found that the best fit for the range of radii used here, which minimised the absolute chi-squared, was a simple linear function, where

$$\Theta(R)/\Theta_0 = (0.186 \pm 0.008)(R/R_0) + (0.887 \pm 0.005) \quad (6)$$

This fit is shown in Figure 8. We emphasize that this fit is specifically intended for the region  $3 \text{ kpc} < R < 8 \text{ kpc}$  and is not a good fit to outer Galaxy rotation. This fit, however, is generalised for applicability to the inner Galaxy in both the first and fourth Galactic quadrants. Although we have assumed  $\Theta_0 = 220 \text{ km s}^{-1}$  in Figure 8, the fit is independent of the assumed values for  $\Theta_0$  and  $R_0$ .

#### 4.3.2. *Velocity Residuals*

From Figure 8 it is clear that there are significant motions that are not fit by this simple rotation curve and the magnitude of these motions should be considered when using this fit for kinematic distances. These residuals give an estimate for the magnitude of streaming motions in the inner Galaxy. Figure 9 shows the residuals for the SGPS and 1st quadrant rotation curves minus the linear fit described above. The peak-to-peak variations in the SGPS residuals using the new fit are  $10 \text{ km s}^{-1}$  and they have a standard deviation of  $5.1 \text{ km s}^{-1}$ . The first quadrant residuals have a larger peak-to-peak variation but this should be confirmed by better sampled data. For comparison, the standard deviation of the SGPS residuals from the Brand & Blitz (1993) fit are  $6.6 \text{ km s}^{-1}$ . The magnitude of these residuals does not differ significantly from those estimated by Shane & Bieger-Smith (1966); Burton (1971) and others, but is perhaps the most well determined estimation available.

That the positions of the bumps in the rotation curve relate to spiral structure has been long known and successfully demonstrated by applications of density wave theory to H I observations of the Milky Way (e.g. Yuan 1969; Burton 1971; Roberts 1969), and other galaxies (e.g. Rots 1975; Visser 1980). Indeed, these bumps are the strongest indicators we have of the locations of the spiral arms. The problem, however, has been that the linear and non-linear versions of the density wave theory predict different relationships between the gravitational centre of a spiral arm and the associated velocity peak. Past data from the Milky Way has not allowed us to distinguish between these two theories, but with the abundance of high resolution H I (McClure-Griffiths et al. 2005; Stil et al. 2006), CO (Luna et al. 2006), and infrared data (Benjamin et al. 2003) for the inner Milky Way now available it may be time to revisit this topic. This will be the topic of a future paper in this series.



## 5. Random Motions Determined From The Terminal Velocity Shape

In addition to providing the offset velocity,  $v_o$ , the shape of the terminal velocity profile provides information about random gas motions in the ISM. The subcentral point is a useful location for measuring these quantities because velocity crowding forces us to observe a large ensemble of H I “clouds”. When we measure the velocity dispersion of H I near the subcentral point we measure a mixture of the microscopic (thermal) and macroscopic (the so-called cloud-to-cloud velocity dispersion) motions. The terminal profile shape is therefore one of the best probes of cloud-to-cloud velocity dispersion in the Galaxy. Our error function fits return values for the velocity widths of the error functions, which are related to the velocity dispersions of the gas as  $\Delta v_i = \sqrt{2}\sigma_v$ . Using the SGPS data beyond the subcentral point we have studied the velocity widths both for the dataset as a whole and as a function of Galactic radius.

In Table 2 we give values for the fitted parameters for two and three component error function fits to the longitude averaged terminal velocity profile. The fitted parameters,  $a_i$ ,  $v_o$  and  $\Delta v_i$ , are those defined in Equation 4. The two component fit parameters are given on the first line of Table 2 and the three component fit parameters are on the second line. The quoted errors are the variation in the parameters that double the reduced  $\chi^2$  of the fit. Note that these errors do not account for co-variance of the fitting parameters. As mentioned in §3.3 and shown in Figure 3 three components produce a significantly better fit to the data, reducing the reduced chi-squared of the fit from over 100 for two components to  $\sim 4$  for three components.

The velocity widths of the two component fit are similar to the Kulkarni & Fich (1985) observations of H I emission towards  $l = 30^\circ$  and  $l = 180^\circ$ , which revealed a narrow component with a velocity dispersion of  $\sigma_v = 6 - 8 \text{ km s}^{-1}$  and a second component with a velocity dispersion of  $15 - 35 \text{ km s}^{-1}$ . Kulkarni & Fich (1985) found that the fits to the broad component were not unique and that values between  $15 \text{ km s}^{-1}$  and  $35 \text{ km s}^{-1}$  fit the data equally well. The H I spectra that Kulkarni & Fich (1985) used were from Weaver & Williams (1973), with an rms noise of  $\sigma_T = 0.38 \text{ K}$ , whereas the SGPS longitude averaged spectrum probes the tail of the H I profile to  $\sigma_T \sim 50 \text{ mK}$ . With the better sensitivity of the longitude averaged SGPS spectrum we can clearly see that the data are better described with three velocity components. Compared to the two component fit, the two narrowest components of the three component fit are smaller. We see that in the three component fit the amplitudes of the first two components are similar and the amplitude of the third component is  $\sim 10\%$  of the first.

That the terminal velocity profile requires three components is perhaps not surprising. H I observed in emission is a mixture of warm ( $T \sim 6000 \text{ K}$ ) and cool ( $T = 50 - 100 \text{ K}$ )

kinetic temperatures. If we ignore the effects of the velocity gradient, the observed velocity dispersion,  $\sigma_v$ , represents a combination of the thermal velocity width,  $\sigma_{th}$ , and the random velocity of the cloud ensemble (cloud-to-cloud motions),  $\sigma_{cc}$ , such that the total velocity width is  $\Delta v = \sqrt{2}\sigma_v = \sqrt{2(\sigma_{th}^2 + \sigma_{cc}^2)}$ . If we assume thermal velocity dispersions for the cold and warm gas of  $\sim 1 \text{ km s}^{-1}$  and  $\sim 7 \text{ km s}^{-1}$ , respectively, then the widths of the two narrow components give cloud-to-cloud velocity dispersions of  $\sim 4.4 \text{ km s}^{-1}$  and  $\sim 5.2 \text{ km s}^{-1}$ , which are identical to within the errors. This suggests that the cold and warm H I share the same bulk motions.

### 5.1. Velocity Dispersion Variations with Galactocentric Radius

Kulkarni & Fich (1985) suggested that the wide velocity dispersion might be related to shocked clouds. For this reason they chose to examine a profile at  $l = 30^\circ$  where the line-of-sight runs tangent to the  $R = 5 \text{ kpc}$  annulus where supernova remnants show a peak. Additionally, Koo and collaborators (i.e. Koo & Kang 2004) have suggested that extended forbidden-velocity line wings may be associated with individual supernova remnants, whose shocks drive H I to high velocities. Given these suggestions it is interesting to explore whether there may be a significant longitude dependence to the velocity dispersion.

Using the full range of the SGPS data we explore whether the velocity widths of the three error functions change with position in the Galaxy. For this analysis we include data in the range  $285^\circ \leq l \leq 340^\circ$ , which excludes data from the inner 3 kpc of the Galaxy where the ISM environment is different from the rest of the disk. We have also excluded data for  $l < 285^\circ$  because at these longitudes the velocity gradient,  $dv/dr$ , is near zero for a particularly long path length, leading to saturation in the H I profiles. Over the longitude range  $285^\circ \leq l \leq 340^\circ$  there are  $\sim 1520$  independent samples. However, to explore the broad velocity component we are interested in brightness temperatures extending as low as  $\sim 250 \text{ mK}$ , so we must average the data into longitude bins of  $\sim 1.4^\circ$  to achieve sufficient signal-to-noise. Note that this analysis necessarily precludes us from finding possible missing supernova remnants by their forbidden-velocity line-wings because we average over large spatial ranges. For each longitude bin we have fit the terminal velocity curve with a sum of three error functions, as defined in Equation 4. The difference between three and two error functions is important here as a fit with only two components produces a consistently wider first component than does the three component fit.

In Figure 10 we plot the widths of the three error functions,  $\Delta v_1(R)$ ,  $\Delta v_2(R)$ , and  $\Delta v_3(R)$  as a functions of galactocentric radius. The error bars are estimated as the variation in the parameter that results in a doubling of the reduced chi-squared. In this plot the three

different symbols correspond to the three different components. The mean values of the three widths are:  $6.5 \pm 2.1 \text{ km s}^{-1}$ ,  $12.8 \pm 3.2 \text{ km s}^{-1}$  and  $25.5 \pm 7.9 \text{ km s}^{-1}$ , which agree well with the values found for the fit to the data averaged over the entire longitude range. We have fit both of the narrowest components as functions of radius, shown in Figure 10. The slope of the narrowest component is consistent with zero:  $\Delta v_1(R) = (6 \pm 1) + (0.2 \pm 0.2)R \text{ km s}^{-1}$ . There is only a very slight slope to the second component, which goes as  $\Delta v_2(R) = (13 \pm 1) - (0.3 \pm 0.2)R \text{ km s}^{-1}$ . The widest component does not show a linear trend but shows a significant increase at small Galactic radii. This increase is accompanied with increasing errors because at large longitudes the tail of the H I emission extends to the edge of the SGPS bandwidth, making it difficult to fit the long tail of the H I profile. Despite the larger errors, the increase appears real.

Burton (1971) also examined the velocity dispersion versus Galactic radius, fitting his single component velocity dispersion with a function of the form  $\sigma(R) = 9 - 0.4R \text{ km s}^{-1}$ . Our fit for the narrowest component is consistent with no gradient in the velocity dispersion across the disk and the middle component shows a shallower slope than Burton’s result. At first our result appears inconsistent with observations of velocity dispersion across the disk of face-on external galaxies, which, like Burton (1971) show that inside the stellar disk the narrow component velocity dispersion increases with decreasing radius (Dickey et al. 1990). The resolution of this apparent conflict, however, may lie in the fact that both studies were based on single component fits, which will produce wide velocity dispersions if the profiles would be better fit by two or three Gaussian components. From our work it seems that the narrow components are effectively constant with radius while the broad component increases with decreasing radius.

In addition to the large-scale trends discussed above, all three components show some small-scale features. At  $R \sim 5 \text{ kpc}$  the wide component increases by a factor of  $\sim 2$  over a width of  $\sim 500 \text{ pc}$ . This increase is also reflected in increases in both of the narrow components. We see that at  $R \sim 6.3 \text{ kpc}$  and  $R \sim 6.8 \text{ kpc}$  the fit effectively reduces to a two component model. It may be noteworthy that the narrowest two components track each other very well with Galactic radius, with all fluctuations observed in both components. This observation supports our suggestion in the previous section that the warm and cold H I share the same bulk motions, which may be either large-scale streaming motions or cloud-to-cloud motions. The separation between the two widths is simply the difference in the thermal motions, not the macroscopic motions which appear to effect warm and cold gas equally.

Some observations of face-on galaxies suggest that there may be some correlation between velocity dispersion and spiral structure (e.g. Braun 1997). Similarly, the original supposition of Kulkarni & Fich (1985) that led them to look for “fast” clouds at  $l = 30^\circ$

was that there may be correlation between fast clouds and areas rich with supernovae, such as spiral arms. At first glance Figure 10 seems to support this latter supposition because all velocity components increase near  $R = 5$  kpc. It is tempting to look deeper into our fitted velocity dispersions for correlation with spiral structure but Burton (1971) reminds us that at the subcentral point the measured velocity dispersion can be related to the path length contributing to the velocities near the subcentral point, in other words the inverse of the velocity gradient,  $|dv/dr|$ . In the presence of streaming motions  $|dv/dr|$  is altered from the value predicted by circular rotation. An increase in velocity dispersion is therefore not necessarily indicative of an increase in the cloud-to-cloud dispersion, but could simply indicate an increase in the path length contributing to the emission near the terminal velocity. Burton showed that for linear density wave theory streaming motions should increase the path length near the terminal velocity just *outside* the spiral arms and suggested that there was an indicative increase in his measured dispersions. However, the Burton (1971) analysis was hampered by single Gaussian fits, which, as he pointed out, were extremely difficult at longitudes where the velocity component became so broad with a flat top that it was better fit by two separate components. Fitting error functions to the tail of the emission beyond the terminal velocity provides some protection against this problem but there is no doubt that in the presence of streaming motions the measured velocity dispersion will change from that measured given purely circular rotation. Unfortunately, once again the *location* of increases relative to spiral structure depends on the density wave theory applied, linear or non-linear. Without knowing the gravitational positions of the spiral arms it is impossible to say whether the increases in velocity width that we observe in all components at  $R \sim 5$  kpc and in the largest component at  $R < 4$  kpc are indicative of a change in  $dv/dr$  or a change in the cloud-to-cloud velocity dispersion.

The velocity gradient also plays a role in the *mixture* of gas-phase components measured beyond the terminal velocity. In the simplest case this can be understood if we consider that for emission beyond the subcentral point and in a given velocity interval,  $\delta v$ , the path length contributing to the emission is  $\delta r = \delta v (dv/dr)^{-1}$ . We can therefore see that for gas with a narrow velocity dispersion only gas very near to the subcentral point contributes to the emission beyond the terminal velocity, whereas gas with a large velocity dispersion can be distributed over a large path length near the subcentral point and still contribute to the emission beyond the terminal velocity. Precisely at the subcentral point the velocity gradient,  $|dv/dr| = 0$  so that it is the second derivative of velocity with distance,  $d^2v/dr^2$ , that determines the distance along the line of sight that contributes to an interval of velocity near the subcentral point as  $\delta r = \sqrt{2 \delta v |d^2v/dr^2|^{-1}}$ , i.e. the second term of a Taylor expansion of  $v(r)$  for  $r \sim r_0$ . The larger the second derivative, the smaller the line of sight contributing to a given spectral interval. Even in pure circular rotation the second derivative of velocity

near the subcentral point changes as a function of longitude so we expect that the proportion of phases represented beyond the terminal velocity will change with longitude. As discussed above, the velocity gradient is also sensitive to streaming motions so understanding the mixture of phases with radius is an extremely complicated issue. We defer that discussion to a future paper, which will explore the spiral structure more fully.

## 6. Conclusions

For the  $\lambda 21$ -cm pioneers who first measured the Milky Way rotation curve 50 years ago, the objective was to determine the radial variation of the gravitational potential, and so to measure the distribution of gravitational mass. In this they were quite successful (Kwee et al. 1954; Schmidt 1956) and only relatively minor adjustments have been made since by breaking the Galaxy down into its disk and spheroidal components (Caldwell & Ostriker 1981). Refinements such as those discussed in this paper do not alter the overall result for the mass of the Galaxy. The significance of the high angular resolution and high precision measurement techniques developed here have more to do with departures from circular rotation than with the overall mass versus radius function. We have fit a new rotation curve to the region  $3 \leq R \leq 8$  kpc using our data from the fourth quadrant together with a previously published rotation curve for the first quadrant. This generalised fit attempts to overcome problems related to quadrant specific fits and is applicable for all of the inner Galaxy. Using this fit we determine the velocity residuals for the fourth quadrant confirming with greater precision that the streaming motions have amplitudes of  $\sim 10 \text{ km s}^{-1}$ . Although the wiggles evident on Figure 9 have long been interpreted in terms of spiral structure their precise location with respect to the gravitational centre of spiral arms is theory dependent. We have future work planned to combine high precision H I and CO surveys with observations of star-forming regions to better quantify the spiral structure in the inner Galaxy.

In addition to large scale variations in the magnitude and direction of the streamlines of the interstellar gas as it rotates around the Galactic Center, some of the small scale fluctuations measured here may be due to non-gravitational perturbations that change the shape of the line profile beyond the terminal velocity. In §3 and §5 we carefully discussed the velocity offset derived from error function fitting to the profile shape beyond the terminal velocity, because the random motions reflected in this shape must be separated from large scale variations in the rotation velocity. Thus in order to trust the interpretation of the wiggles on Figure 9 as being due to spiral arms, we must first eliminate wiggles in  $v_o$  similar to those in  $\Delta v_1$ ,  $\Delta v_2$ , and  $\Delta v_3$  on Figure 10.

We have presented a successful technique for measuring the terminal velocity of H I

in the inner Galaxy. As shown in Figures 4 and 5, the technique of fitting complementary error functions to the H I terminal velocity is quite robust, giving results that are consistent to less than the width of one velocity channel over much of the longitude range of the survey. Our technique is effective at overcoming the biases that might be introduced by determining the terminal velocity using brightness temperature threshold methods. Our fits show that H I terminal velocities estimated based on a brightness temperature threshold without any correction will over-estimate the terminal velocity by 5 – 10 km s<sup>-1</sup>. Although the CO velocity dispersion is smaller than for H I, terminal velocities estimated from CO emission using a threshold technique are also not immune from over-estimation by amounts comparable to molecular cloud velocity dispersion. Comparison of the H I and Luna et al. (2006) <sup>12</sup>CO terminal velocities has shown that the CO velocities have more scatter than those presented here from H I. We attribute some of this difference to the different volume filling factors of H I and CO and suggest that H I measurements of the terminal velocity may be more robust than CO because they detect a larger ensemble of clouds.

The technique of fitting the H I terminal velocity profile has the added benefit that it returns information about the velocity width of the H I beyond the terminal velocity. The fitted velocity width combines information about the thermal width of the gas, the inherent velocity dispersion as caused by cloud-to-cloud motions, and changes in the velocity gradient, which may be caused by streaming motions associated with spiral arms. Unravelling these effects at specific positions within the inner Galaxy is complicated and something we hope to address in a future paper. Averaging over all longitudes to mitigate against local variations in the velocity gradient we have shown that the H I terminal velocity shape is best fit by the combination of three error functions, with widths of 6 km s<sup>-1</sup>, 12 km s<sup>-1</sup>, and 26 km s<sup>-1</sup>. Examining the three velocity widths as a function of Galactic radius we found that the widths of the narrower two components track each other very well at all Galactic radii and show no appreciable trend with radius. We suggest that the agreement between the narrow components is evidence that the two thermal phases share the same bulk motions as well as variations in the velocity gradient. Unlike the two narrow components, the third, widest, component appears to increase with decreasing Galactic radius for  $R < 4$  kpc. It is unclear at this time whether this increase reflects a true increase in the cloud-to-cloud motions or streaming motions.

This research was supported in part by NSF grants AST-9732695 and AST-0307603 to the University of Minnesota. We greatly appreciate the involvement and advice of B. M. Gaensler and A. J. Green with the original SGPS observations and all subsequent analysis. NMMc-G acknowledges D. McConnell for suggestions related the automated error function fitting of H I profiles and A. Luna for providing the CO terminal velocities in tabulated

form. Both NMMc-G and JMD acknowledge comments and suggestions by W. B. Burton on a previous version of this manuscript. We would particularly like to thank E. Levine and the referee, F. J. Lockman, for excellent questions and suggestions.

## REFERENCES

- Alvarez, H., May, J., & Bronfman, L. 1990, *ApJ*, 348, 495
- Anantharamaiah, K. R., Radhakrishnan, V., & Shaver, P. A. 1984, *A&A*, 138, 131
- Benjamin, R. A., Churchwell, E., Babler, B. L., Bania, T. M., Clemens, D. P., Cohen, M., Dickey, J. M., Indebetouw, R., Jackson, J. M., Kobulnicky, H. A., Lazarian, A., Marston, A. P., Mathis, J. S., Meade, M. R., Seager, S., Stolovy, S. R., Watson, C., Whitney, B. A., Wolff, M. J., & Wolfire, M. G. 2003, *PASP*, 115, 953
- Binney, J. & Tremaine, S. 1987, *Galactic Dynamics* (Princeton: Princeton University Press)
- Blitz, L. & Spergel, D. N. 1991, *ApJ*, 370, 205
- Brand, J. & Blitz, L. 1993, *A&A*, 275, 67
- Braun, R. 1997, *ApJ*, 484, 637
- Burton, W. B. 1971, *A&A*, 10, 76
- . 1976, *ARA&A*, 14, 275
- Burton, W. B. & Gordon, M. A. 1978, *A&A*, 63, 7
- Burton, W. B. & Liszt, H. S. 1993, *A&A*, 274, 765
- Caldwell, J. A. R. & Ostriker, J. P. 1981, *ApJ*, 251, 61
- Celnik, W., Rohlfs, K., & Braunsfurth, E. 1979, *A&A*, 76, 24
- Clemens, D. P. 1985, *ApJ*, 295, 422
- Dawson, J., Kawamura, A., & Fukui, Y. 2006, in *IAU Symposium*
- Dickey, J. M., Hanson, M. M., & Helou, G. 1990, *ApJ*, 352, 522
- Dickey, J. M. & Lockman, F. J. 1990, *ARA&A*, 28, 215
- Eisenhauer, F., Genzel, R., Alexander, T., Abuter, R., Paumard, T., Ott, T., Gilbert, A., Gillessen, S., Horrobin, M., Trippe, S., Bonnet, H., Dumas, C., Hubin, N., Kaufer, A., Kissler-Patig, M., Monnet, G., Ströbele, S., Szeifert, T., Eckart, A., Schödel, R., & Zucker, S. 2005, *ApJ*, 628, 246

- Ferrière, K. M., Gillard, W., & Jean, P. 2007, *A&A*, in press
- Fich, M., Blitz, L., & Stark, A. A. 1989, *ApJ*, 342, 272
- Grabelsky, D. A., Cohen, R. S., Bronfman, L., Thaddeus, P., & May, J. 1987, *ApJ*, 315, 122
- Gunn, J. E., Knapp, G. R., & Tremaine, S. D. 1979, *AJ*, 84, 1181
- Haverkorn, M., Gaensler, B. M., McClure-Griffiths, N. M., Dickey, J. M., & Green, A. J. 2006, *ApJS*, 167, 230
- Henderson, A. P., Jackson, P. D., & Kerr, F. J. 1982, *ApJ*, 263, 116
- Humphreys, R. M. & Kerr, F. J. 1974, *ApJ*, 194, 301
- Kerr, F. J. 1962, *MNRAS*, 123, 327
- Koo, B.-C. & Kang, J.-h. 2004, *MNRAS*, 349, 983
- Kulkarni, S. R. & Fich, M. 1985, *ApJ*, 289, 792
- Kwee, K. K., Muller, C. A., & Westerhout, G. 1954, *Bull. Astron. Inst. Netherlands*, 12, 211
- Lin, C. C., Yuan, C., & Roberts, Jr., W. W. 1978, *A&A*, 69, 181
- Lin, C. C., Yuan, C., & Shu, F. H. 1969, *ApJ*, 155, 721
- Liszt, H. S. 1983, *ApJ*, 275, 163
- Luna, A., Bronfman, L., Carrasco, L., & May, J. 2006, *ApJ*, 641, 938
- Malhotra, S. 1995, *ApJ*, 448, 138
- McClure-Griffiths, N. M., Dickey, J. M., Gaensler, B. M., Green, A. J., Haverkorn, M., & Strasser, S. 2005, *ApJS*, 158, 178
- Mignard, F. 2000, *A&A*, 354, 522
- Press, W. H., Flannery, B. P., Teukolsky, S. A., & Vetterling, W. T. 1992, *Numerical Recipes in Fortran* (Cambridge University Press)
- Radhakrishnan, V. & Srinivasan, G. 1980, *Journal of Astrophysics and Astronomy*, 1, 47
- Reid, M. J. 1993, *ARA&A*, 31, 345
- Roberts, W. W. 1969, *ApJ*, 158, 123
- Rots, A. H. 1975, *A&A*, 45, 43
- Schmidt, M. 1956, *Bull. Astron. Inst. Netherlands*, 13, 15



- Shane, W. W. & Bieger-Smith, G. P. 1966, *Bull. Astron. Inst. Netherlands*, 18, 263
- Sinha, R. P. 1978, *A&A*, 69, 227
- Stil, J. M., Taylor, A. R., Dickey, J. M., Kavars, D. W., Martin, P. G., Rothwell, T. A., Boothroyd, A. I., Lockman, F. J., & McClure-Griffiths, N. M. 2006, *AJ*, 132, 1158
- van Woerden, H., Rougoor, G. W., & Oort, J. H. 1957, *Comp. Rendu* 244, 1961
- Visser, H. C. D. 1980, *A&A*, 88, 149
- Weaver, H. & Williams, D. R. W. 1973, *A&AS*, 8, 1
- Yuan, C. 1969, *ApJ*, 158, 871

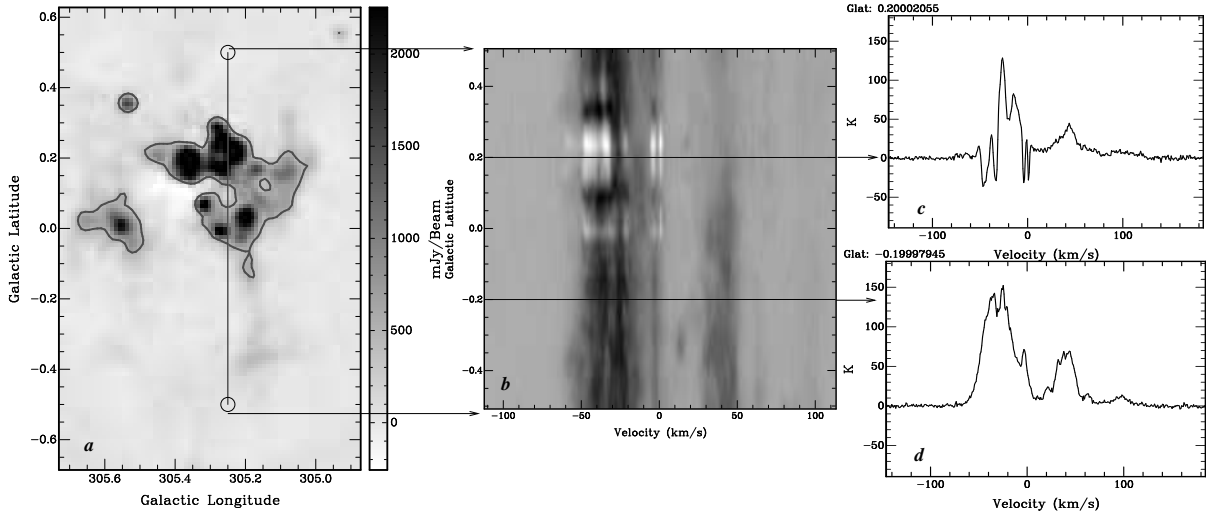


Fig. 1.— An illustration of the effect of continuum absorption on the H I spectra. The left hand panel shows a grey scale map of continuum sources near longitude  $l = 305^{\circ}25$ . The vertical line spanning  $+0^{\circ}.5 \geq b \geq -0^{\circ}.5$  shows the area covered in a single latitude average. The latitude-velocity plot in the center panel shows the H I line intensity along this line, with velocity as the horizontal axis and grey scale indicating brightness temperature. The white areas have  $T_B < 0$  because the continuum has been subtracted from the spectral line cubes. The right hand panels show two spectra, at  $b = +0^{\circ}.2$  and  $b = -0^{\circ}.2$ , sliced from the latitude velocity plot. The upper one is polluted by absorption toward the continuum and must be excluded from the calculations.

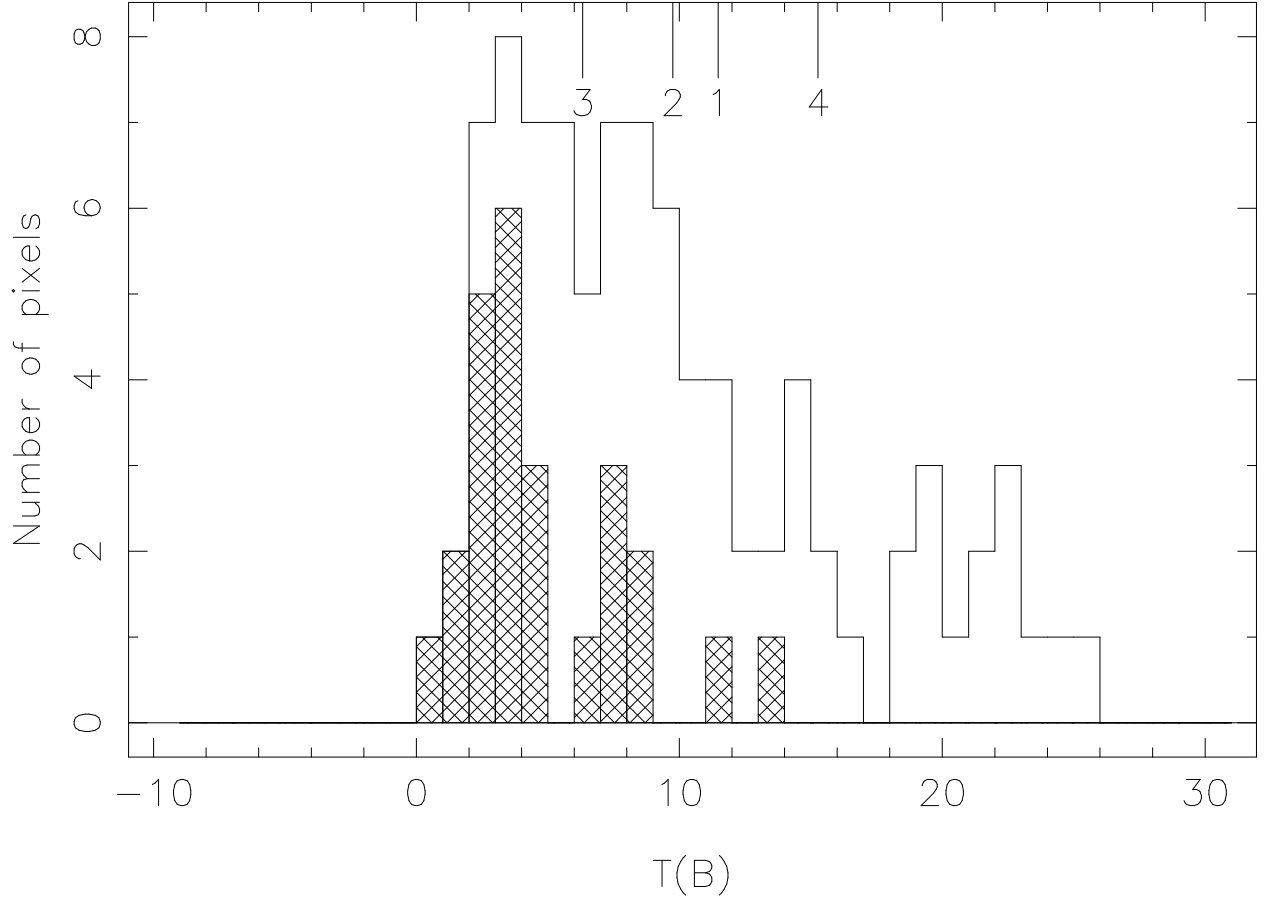


Fig. 2.— Distribution function of the brightness temperature measured at  $v = -61.83$   $\text{km s}^{-1}$ ,  $l = 305^{\circ}25$ , for latitudes  $+0^{\circ}5 \geq b \geq -0^{\circ}5$ , which is the range shown on Figure 1. The velocity displayed here is the threshold crossing velocity for this longitude, meaning it is the most negative velocity for which the mean of the brightness temperature distribution is above the 10 K threshold. The mean, median, 25th percentile, and 75th percentile of the distribution are indicated by the marks labelled 1, 2, 3, and 4 respectively. The shaded pixels are eliminated from the distribution before computing the statistics because they correspond to positions where the continuum is above the cutoff of 0.5 K. Distribution functions like this are analysed at every longitude, and the four statistics are used to compute four alternative velocity shifts,  $v_t(l)$ , where each one crosses the 10 K threshold.

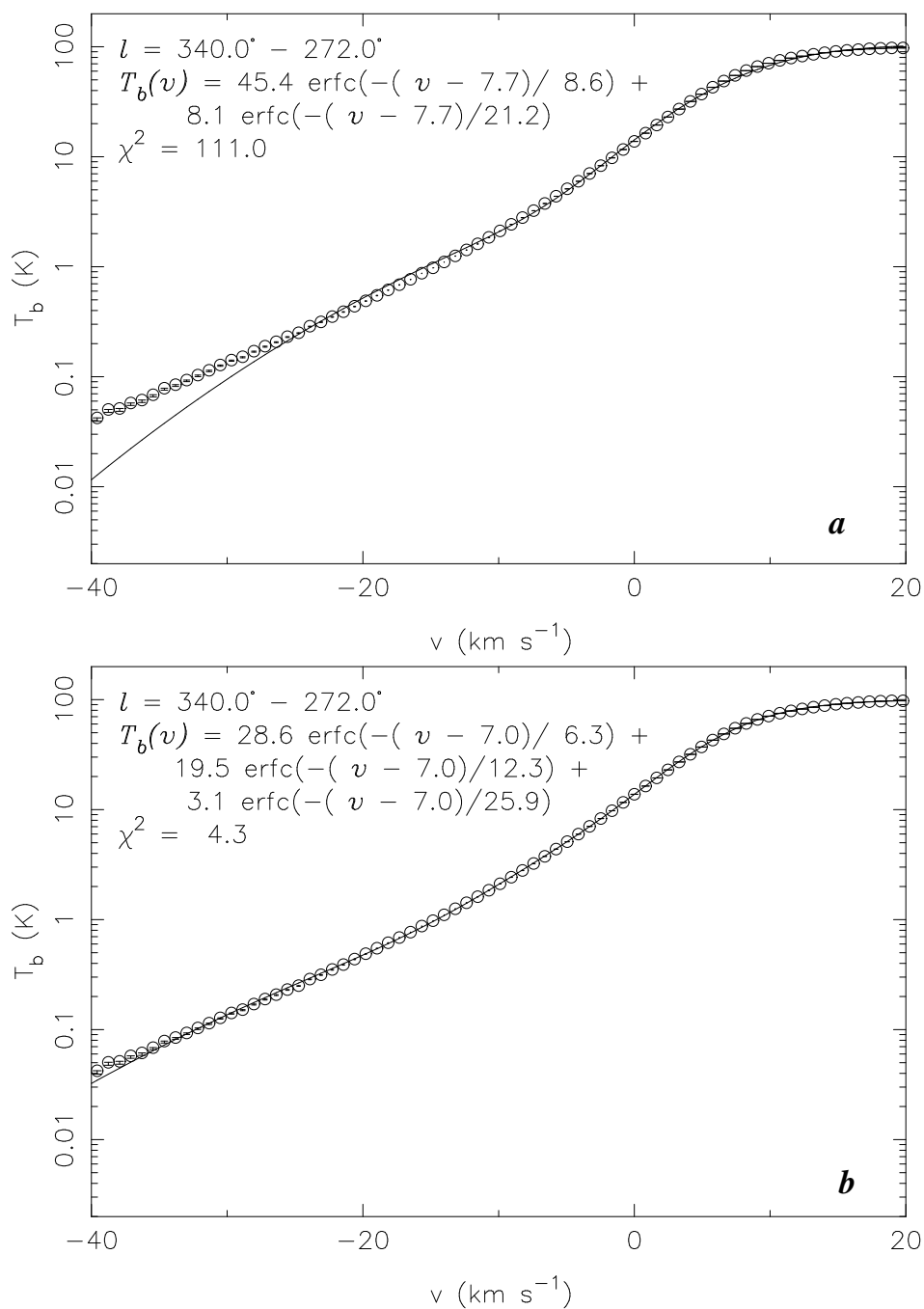


Fig. 3.— Error function fits to the longitude averaged terminal velocity profile. Panel *a* shows a two component fit to the profile while panel *b* shows a three component fit to the profile. Clearly the three component fit is much better able to account for the tail of the profile.

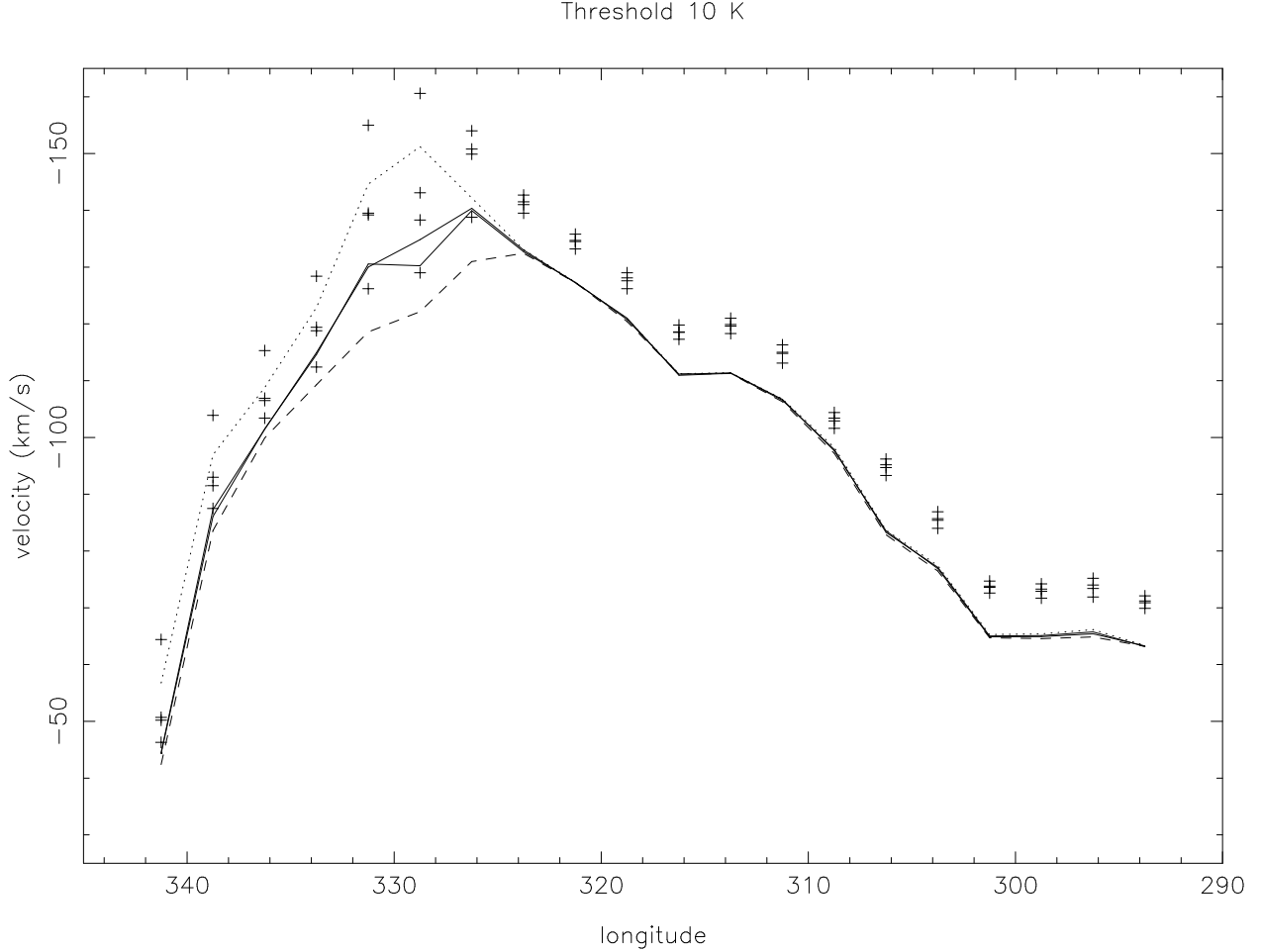


Fig. 4.— The effect of correcting the threshold crossing velocity by  $v_o$ , the velocity offset from the error function fits. The four crosses at each longitude are the average values of  $v_t$  in each longitude interval ( $2.5^\circ$ ), for the four statistics (mean, median, 25th and 75th percentile) used to find the threshold crossings. The 25th percentile gives consistently lower negative velocity values, while the 75th percentile gives higher values, while the mean and median give values of  $v_t$  that are generally quite close together. But after adding the corresponding  $v_o$  all the values agree much better, as indicated by the curves that join values of  $v_{LSR}$  for each longitude bin. The dotted curve is for the 75th percentile, the dashed curve for the 25th percentile, and the two solid curves are for the mean and median. All four agree to better than  $0.5 \text{ km s}^{-1}$  for longitudes less than about  $l = 325^\circ$ , as discussed in the text.

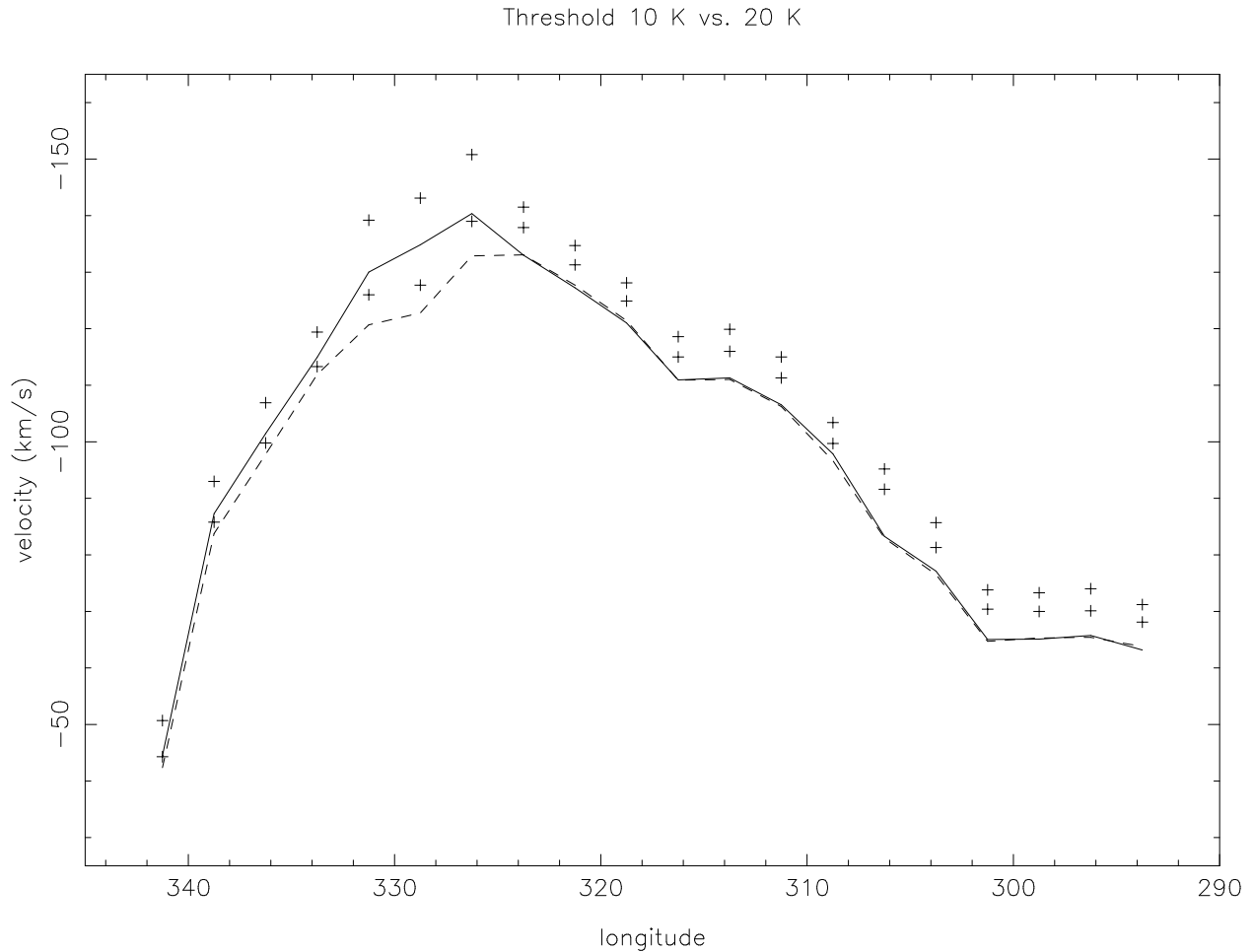


Fig. 5.— The difference between choosing thresholds of 10 K and 20 K in brightness temperature. As on Figure 4 the crosses show the threshold crossing velocities, this time for the two thresholds both using the mean value (average over latitude) as the statistic. The higher negative velocities correspond to the lower threshold, as shown on fig. 4. After applying the correction  $v_o$  found from erfc fitting, the two thresholds give the same result to less than  $0.5 \text{ km s}^{-1}$  for longitudes less than  $325^\circ$ , as discussed in the text. This demonstrates that the final function  $v_{LSR}(l)$  is independent of the arbitrary choice of threshold over most of the longitude range of the survey.

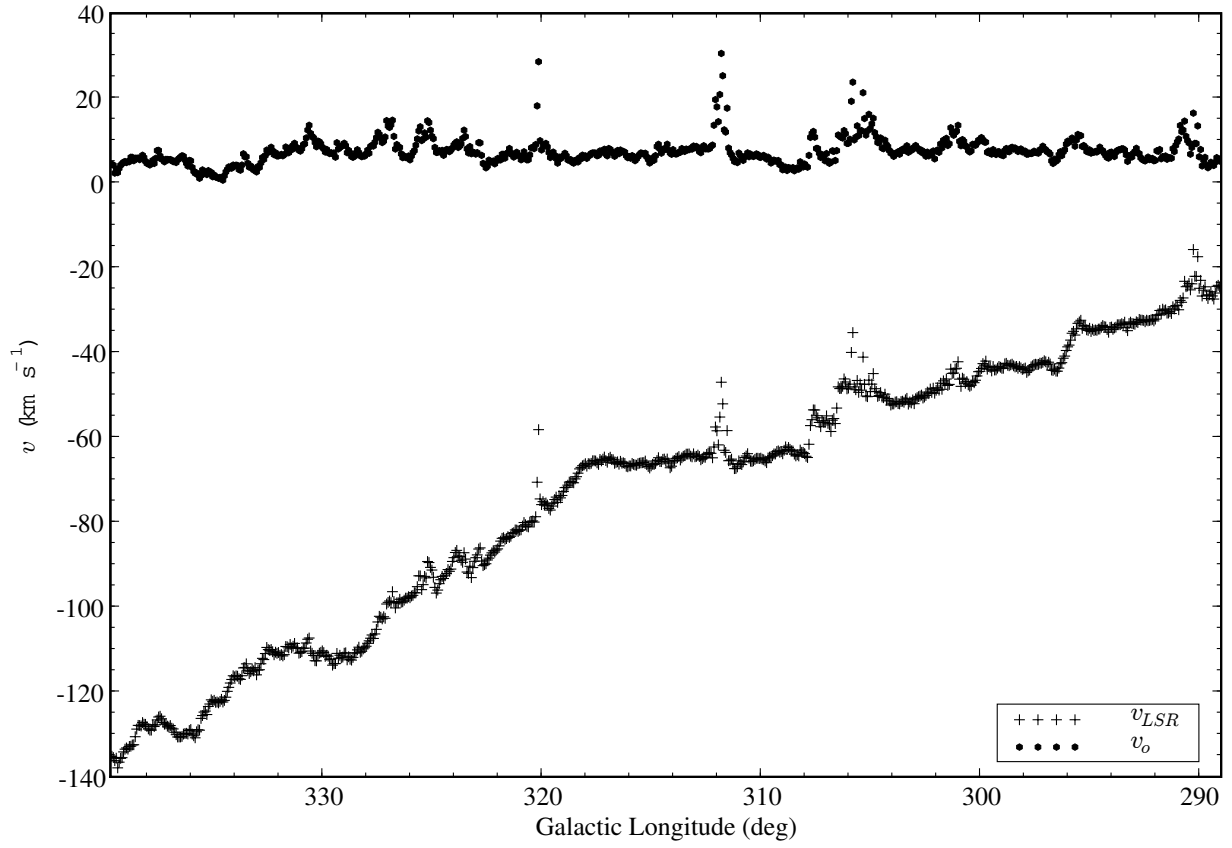


Fig. 6.— H I terminal velocities,  $v_{LSR}$ , and the offset velocity,  $v_o$ , versus Galactic longitude for the fourth quadrant of the Milky Way.

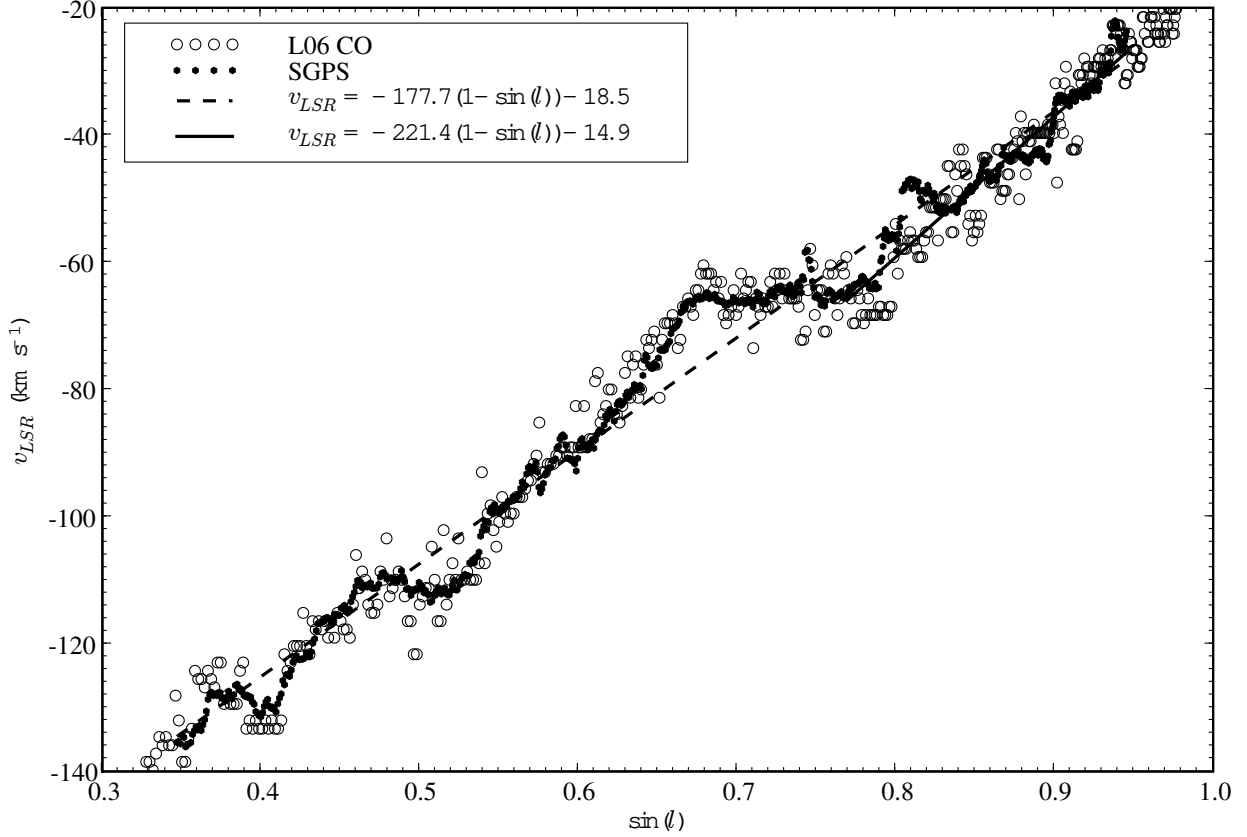


Fig. 7.— H I and CO terminal velocities versus  $|\sin l|$  for the fourth quadrant of the Milky Way. CO terminal velocities are from Luna et al. (2006)[L06]. The H I terminal velocities have been fit with a linear function of the form  $v_{LSR} = \Theta_0(|\sin l| - 1) + v'$ . The slope of the fit is dependent on the range of  $\sin l$  used in the fitting. The dashed line shows a fit over the range  $0.35 \leq |\sin l| \leq 0.95$  and the solid line shows the fit over the restricted range  $0.8 \leq |\sin l| \leq 0.95$ . The fitted values are given in the legend.



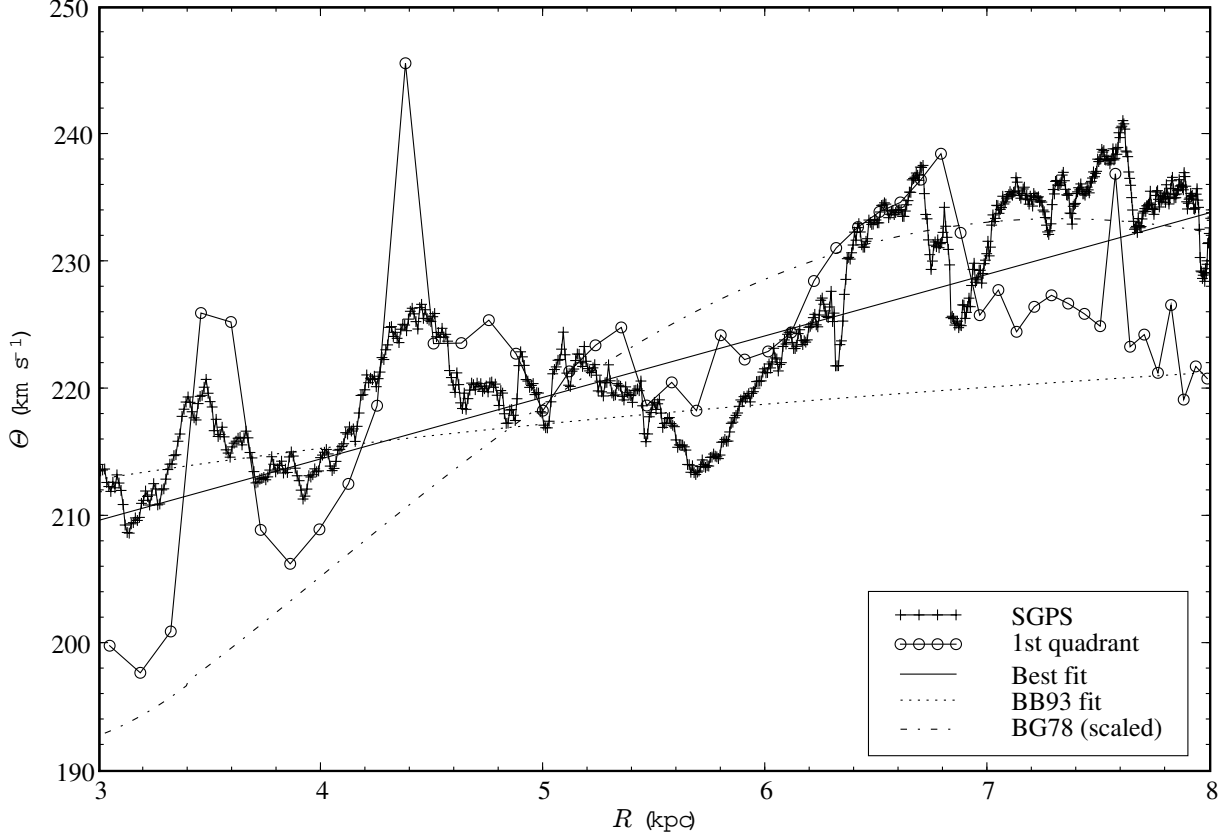


Fig. 8.— Rotation curve for the fourth quadrant of the Milky Way interior to the Solar circle. The crosses are the SGPS data points and the open circles are the first quadrant values from Fich et al. (1989). Error bars are not shown on this plot to reduce confusion. Estimates of the errors are included in the fitting and are  $4.6$  for  $l > 0^\circ$  (Fich et al. 1989),  $1 \text{ km s}^{-1}$  for  $l < 325^\circ$ ,  $3 \text{ km s}^{-1}$  for  $l > 332.5^\circ$  and  $10 \text{ km s}^{-1}$  for  $327.5^\circ \leq l \leq 332^\circ$ , as described in the text. The dotted line is the commonly used Brand & Blitz (1993) rotation curve derived for the outer Galaxy. The dashed-dotted line is the Burton & Gordon (1978) polynomial fit to the first quadrant rotation curve. This fit has been scaled from the original assumption of  $R_0 = 10 \text{ kpc}$  and  $\Theta_0 = 250 \text{ km s}^{-1}$  to  $R_0 = 8.5 \text{ kpc}$  and  $\Theta_0 = 230 \text{ km s}^{-1}$ . We found it necessary to use  $\Theta_0 = 230 \text{ km s}^{-1}$  rather than  $220 \text{ km s}^{-1}$  to place the peak near the observe peak velocities. The solid line is the best fit to the ensemble of the first and fourth quadrant (SGPS) data over the range  $3 \leq R \leq 8 \text{ kpc}$  given by  $\Theta(R)/\Theta_0 = 0.186 \pm 0.008(R/R_0) + 0.887 \pm 0.005$ , where  $\Theta_0 = 220 \text{ km s}^{-1}$  and  $R_0 = 8.5 \text{ kpc}$ .

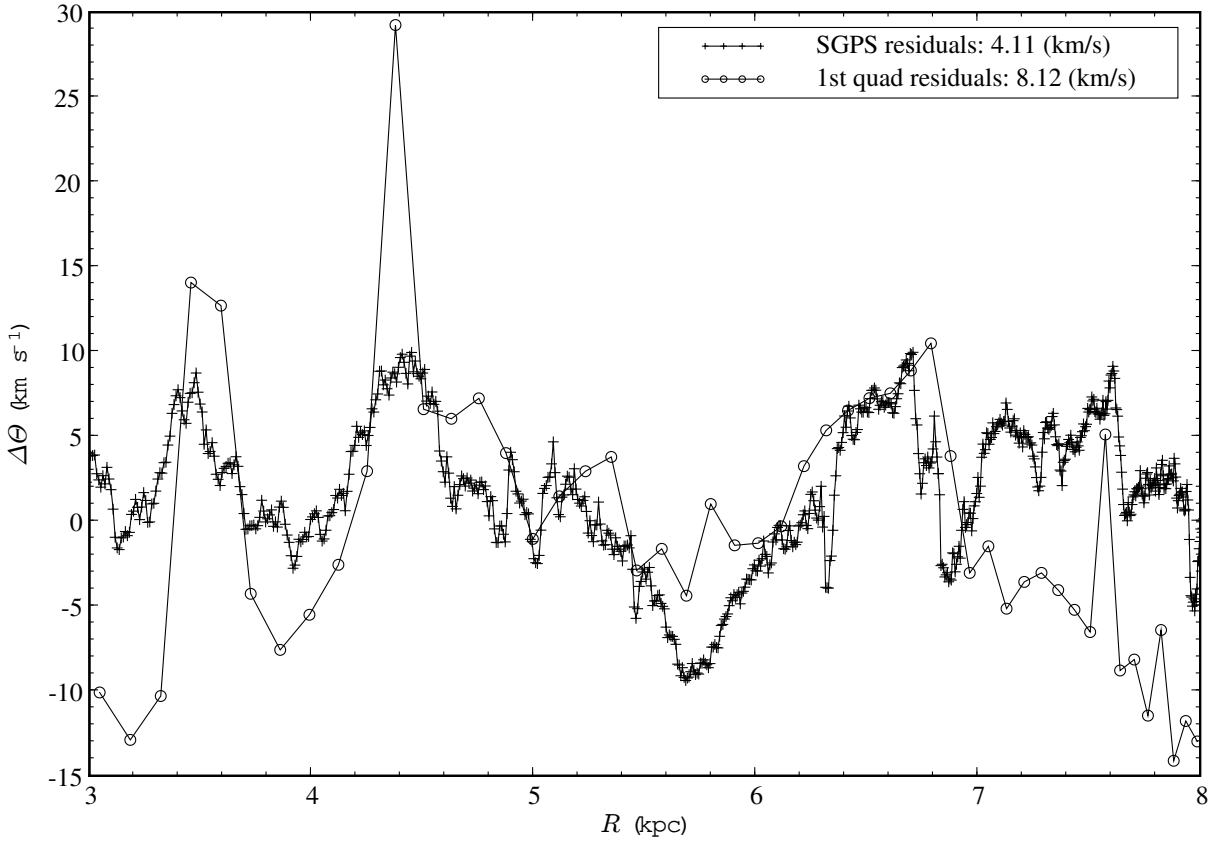


Fig. 9.— Residuals from the rotation curve fit presented in Figure 8. The standard deviation for the SGPS residuals is  $4.11 \text{ km s}^{-1}$ , whereas the standard deviation for residuals from the Brand & Blitz (1993) curve was  $6.6 \text{ km s}^{-1}$ .

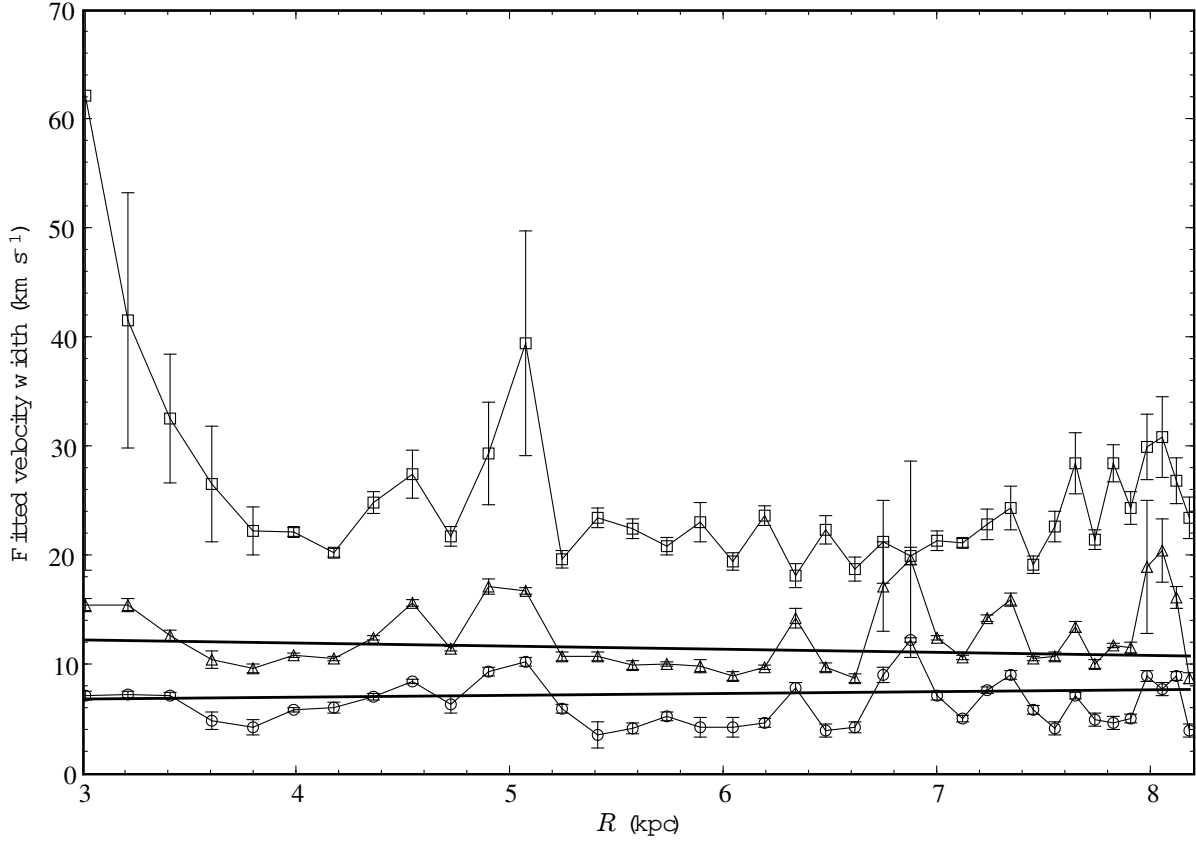


Fig. 10.— Widths of the three velocity components fitted to the terminal velocity profile as a function of Galactic longitude. These data are binned by  $1^{\circ}4$  of Galactic longitude. The plotting symbols for the narrow, middle and wide components are circles, triangles and boxes, respectively. The error bars are the amount of variation in a parameter required to double the chi-squared of the fit. The narrowest components are fit with linear functions of the form  $\Delta v_1(R) = (6 \pm 1) + (0.2 \pm 0.2)R \text{ km s}^{-1}$  and  $\Delta v_2(R) = (13 \pm 1) - (0.3 \pm 0.2)R \text{ km s}^{-1}$ .

Table 1. Measured H I terminal velocities,  $v_{LSR}$ , as a function of Galactic longitude,  $l$ , from the SGPS. The third column gives the terminal velocities,  $v_{mod}$ , predicted by the rotation curve defined in Equation 6. Note– the full version of this table appears in the electronic edition of the Journal, an abbreviated form is presented here.

$l$ (deg)	$v_{LSR}$ (km s <sup>-1</sup> )	$v_{mod}$ (km s <sup>-1</sup> )
339.695	-135.22	-133.00
339.628	-135.14	-132.80
339.562	-135.44	-132.61
339.495	-136.17	-132.41
339.428	-135.59	-132.22
339.362	-137.87	-132.02
339.295	-136.53	-131.83
339.228	-135.63	-131.63
339.162	-135.47	-131.44
339.095	-134.11	-131.24

Table 2. Fitted values for velocity widths of two and three component error function fits to the terminal velocity curve averaged over the longitude range  $272^\circ \leq l \leq 340^\circ$ .

	$v_o$ (km s <sup>-1</sup> )	$a_1$ (K)	$\Delta v_1$ (km s <sup>-1</sup> )	$a_2$ (K)	$\Delta v_2$ (km s <sup>-1</sup> )	$a_3$ (K)	$\Delta v_3$ (km s <sup>-1</sup> )
2-component fit	$7.7 \pm 0.3$	$45.4 \pm 3.6$	$8.6 \pm 0.3$	$8.1 \pm 0.8$	$21.2 \pm 1.3$		
3-component fit	$7.0 \pm 0.1$	$28.6 \pm 1.1$	$6.3 \pm 0.1$	$19.5 \pm 0.4$	$12.3 \pm 0.3$	$3.1 \pm 0.1$	$25.9 \pm 0.5$